People's Democratic Republic of Algeria

Ministry of Higher Education and Scientific Research

University M'Hamed BOUGARA- Boumerdes

Institute of Electrical and Electronic

Engineering Department of Power and Control

Engineering

Project Report Presented in Partial Fulfilment of

the Requirements of the Degree of

'MASTER'

In Electrical and Electronic engineering

Option: Power Engineering

Title:

Bearing Faults Classification of Induction Motor Using Advanced Deep Learning Techniques.

Presented By:

Seyyid Ahmed DJELOULI

Supervisors:

Pr. KHELDOUN. A

Co-supervisor:

Dr. DJEDDI. M

Registration Number... /2024

Acknowledgments

I would like to express my deepest gratitude to everyone who has been instrumental in this journey.

To my supervisors, your guidance, wisdom, and encouragement have been invaluable. Your belief in my potential and dedication to my success have been a constant source of motivation. Thank you for your unwavering support and for challenging me to strive for excellence.

To my family, your love and support have been the bedrock of my life. You have been my inspiration and my refuge. Thank you for your patience, understanding, and for always believing in me, even when the path was uncertain.

To God, whose grace and blessings have provided me with strength and direction. Your presence in my life has been a guiding light, and I am forever grateful for the countless blessings that have enabled me to pursue and achieve my dreams.

As I look forward to the future, I carry with me the lessons learned and the support received. I wish for a future filled with growth, opportunities, and the continued pursuit of knowledge and innovation. Thank you all for being a part of this incredible journey.

Abstract

This study investigates the application of advanced neural network models for bearing fault detection using vibration and current signals. Bearing faults in induction motors pose significant challenges to industrial operations, often leading to unexpected downtimes and increased maintenance costs. The study explores the performance of Artificial Neural Networks (ANN), 1D-Convolutional Neural Networks (1D-CNN), 1D-CNN with multi-kernel sizes, and Long Short-Term Memory (LSTM) models. Findings indicate that 1D-CNN and its multi-kernel size variant outperform other models, achieving accuracies up to 99.95% under various load conditions for vibration data. The 1D-CNN multi-kernel size model's ability to capture diverse features through different kernel sizes proved advantageous, reflecting a significant improvement over previous methodologies that relied on extensive preprocessing.For the current signal dataset,Our recent findings surpass all prior results, particularly in variable speed operation, where our work marks a pioneering effort. In our current signal dataset, the pinnacle of accuracy, reaching 99.88%, was attained through the application of the 1D-CNN model with the variable load operation dataset. This remarkable success highlights the effectiveness of merging 1D-CNN with Variational Mode Decomposition (VMD), enabling the proficient decomposition of signals and resolution of boundary effects to handle intricate fault patterns.

Despite encountering greater complexities in variable speed operation, our models persevered and achieved commendable accuracies. Notably, the 1D-CNN model achieved an accuracy of up to 99.36%. These results highlights the significant achievement made in terms of diagnosis in induction motors.

List of Abbreviations and Terms

ADMM	Alternate Direction Method of Multipliers
AI	Artificial intelligence
AM	Amplitude Modulated
ANN	Artificial Neural Networks
BPTT	Back-Propagation Through Time
CNN	Convolutional Neural Networks
CNN-MKS	Convolutional Neural Networks with Multi Kernel Size
CT	Current Transformer
CWRU	Case Western Reserve University
CWT	Continuous Wavelet Transform
DWT	Discrete Wavelet Transform
EA	Envelope Analysis
EPRI	Electric Power Research Institute
FDA	Frequency Domain Analysis
FFT	Fast Fourier Transform
FM	Frequency Modulated
HFRT	High-Frequency Resonance technique
HHT	Hilbert Huang Transform
HP	Horsepower
IEEE	Institute of Electrical and Electronics Engineering
IMFs	Intrinsic Mode Functions

ISO	International Organization for Standardization
IQR	Interquartile range
LSTM	Long Short-Term Memory
MSE	Mean Squared Error
NM	Newton-metre
PCA	Principal Component Analysis
REBs	Rotating Equipment Bearings
RMS	Root Means Square
RNN	Recurrent Neural Network
SGD	Stochastic Gradient Descent
SMOTE	Synthetic Minority Over-sampling Technique
STFT	Short-time Fourier Transform
TFDA	Time-Frequency Domain Analysis
T-SNE	T-distributed Stochastic Neighbor Embedding
VMD	Variational Mode Decomposition
WPT	Wavelet Packet Transform
WT	Wavelet Transform
WVD	Wigner-Ville Distribution

Contents

List of Figures

List of Tables

General Introduction

General Introduction

Bearing faults are a critical issue in induction motors, leading to costly downtimes and potential safety hazards. The primary causes of bearing faults include improper installation, inadequate lubrication, and material fatigue, which can result in vibration, noise, and ultimately machinery failure. Over the years, the detection and classification of bearing faults have evolved significantly, with advancements in signal processing techniques and artificial intelligence (AI) playing a crucial role. Initially, simple time-domain analysis was used to identify faults, but this approach often lacked accuracy and sensitivity. As technology progressed, more sophisticated methods like frequency-domain and time-frequency domain analyses, such as Fast Fourier Transform (FFT) and Wavelet Transform, were employed to enhance fault detection capabilities.

In recent years, AI and machine learning algorithms have been increasingly integrated with these signal processing techniques, offering more accurate and reliable fault diagnosis. Commonly used signals for bearing fault detection include vibration, acoustic emission, and motor current signals. Vibration signals are particularly popular and effective due to their high sensitivity to bearing faults and ease of acquisition. Acoustic emission signals, while also highly sensitive and capable of detecting early-stage faults, are more challenging to capture and interpret.

Motor current signals offer a non-intrusive means of fault detection but can be less sensitive compared to vibration and acoustic emission signals. This interdisciplinary approach combining signal processing and AI not only improves fault detection accuracy but also enables early intervention, thereby extending the lifespan of machinery and enhancing operational efficiency. The aim of this work is to explore new promising methods to detect and classify bearing faults using a combination of signal processing approaches and artificial intelligence techniques to solve this challenge.

This study is divided into four chapters: Chapter One provides an introduction to induction motors, covering their construction, operation, and fault analysis. Chapter Two reviews the state of the art in bearing fault detection methods for induction motors. Chapter Three describes the dataset used in the study. Chapter Four details the experiments conducted on bearing fault classification and discusses the obtained results.

Chapter 1

Induction motors: Construction, Operation, and Faults.

Introduction

This chapter provides a comprehensive overview of an induction motor, starting with its construction and then delving into its various faults.As an Initial topic, the construction of induction motor is discussed hereafter. This is followed by an analysis of faults commonly found in induction motors. The discussion includes faults such as broken rotor bars, mass imbalance, stator faults, single phasing and bearing faults. Each fault is explored in detail, with a focus on its causes and consequences.

1.1 Structure of induction motors

An induction motor is made up of a magnetic circuit that connects two electrical circuits. These circuits are located in the two primary components of the machine: (i) the stator, and (ii) the rotor. Power is transferred from one component to the other through electromagnetic induction. This is why the induction machine is often referred to as an electromechanical energy conversion device - it transforms electrical energy into mechanical energy [1]. The rotor is held in place by bearings at both ends. Typically, both the stator and rotor have two circuits: (a) an electrical circuit, which carries the current, and (b) a magnetic circuit, which carries the magnetic flux. The induction

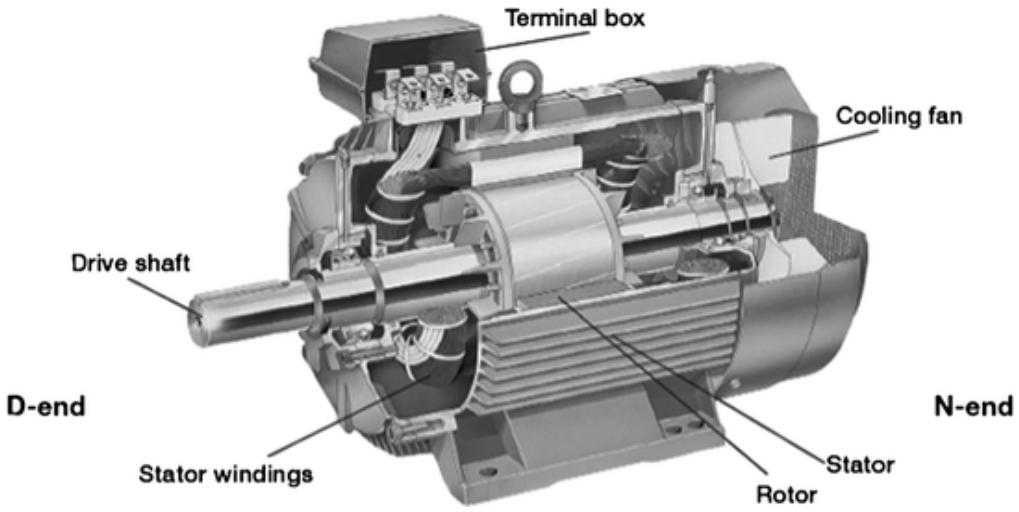

Figure 1.1: An induction motor dissected into its main components [2]

motor, a cornerstone of electromechanical engineering, transforms electrical energy into mechanical

power through electromagnetic induction. Within its stator and rotor lie two essential circuits: an electrical circuit, typically comprising insulated copper or aluminum for current conduction, and a magnetic circuit, commonly constructed from laminated steel to facilitate flux transmission. Bearings ensure the rotor's stability for smooth rotation. This harmonious integration of magnetic and electrical components not only illustrate the motor's efficiency but also underscores its versatility across diverse applications, from industrial machinery to household appliances.

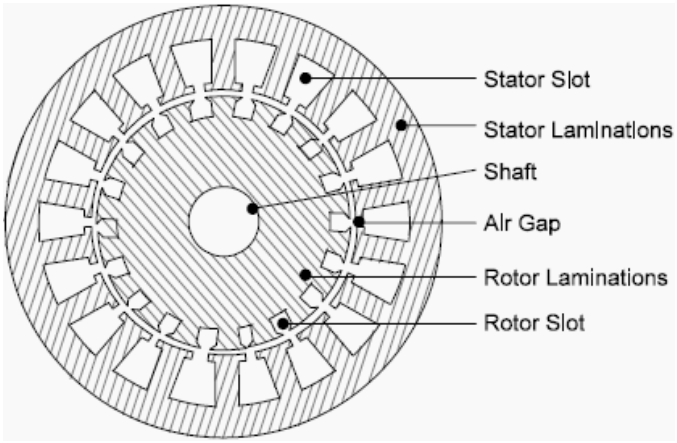

Figure 1.2: Magnetic circuit of stator and rotor of an induction motor[2]

1.2 Construction

1.2.1 Stator

The stator, as depicted in Figure 1.3, constitutes the stationary outer component of the motor and comprises three primary constituents: the outer cylindrical frame, the magnetic path, and a collection of insulated electrical windings.

1.2.1.1 Outer cylindrical frame

Composed of either cast iron, cast aluminum alloy, or welded fabricated sheet steel, the frame facilitates motor mounting, typically featuring [correction(feet for foot)] mounting or a flange for alternative mounting arrangements.

1.2.1.2 Magnetic path

Comprising a series of slotted high-grade alloy steel laminations embedded within the outer cylindrical stator frame, the magnetic path serves to optimize magnetic flux distribution. Lamination of the path minimizes losses due to eddy currents and heat generation.

1.2.1.3 Set of insulated electrical windings

In the case of a 3-phase motor, the stator circuit encompasses three distinct sets of coils, each corresponding to a phase. Positioned at intervals of 120 degrees within the slots of the laminated magnetic path, these coils are energized by a three-phase power supply, enabling motor operation.

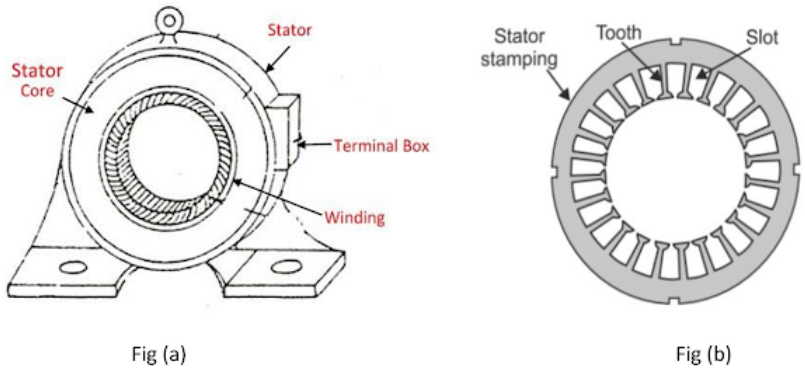

Figure 1.3: Stator of an induction motor [3]

1.2.2 Rotor

The rotor, serving as the rotating component of the motor, resides within the stator bore and rotates in alignment with it.The rotor is comprised of a series of slotted thin sheets known as laminations, made from electromagnetic material (specifically core steel), forming a cylinder when pressed together. These sheets are insulated from one another using materials such as paper and varnish[4]. Within the rotor, the slots define the electrical circuit, while the cylindrical electromagnetic material serves as the magnetic path. The rotor winding of an induction motor may manifest

in two primary forms: the squirrel-cage type and the wound type, thereby categorizing induction motors into two groups:

1.2.2.1 Squirrel-cage type induction motor

This type of motors has a rotor configuration features a set of bars crafted from copper, aluminum, or alloy, serving as rotor conductors embedded within the rotor slots. This design ensures robust rotor construction, with the rotor bars interconnected at both ends to form a closed loop. Figure 1.4 illustrates a squirrel-cage type rotor.

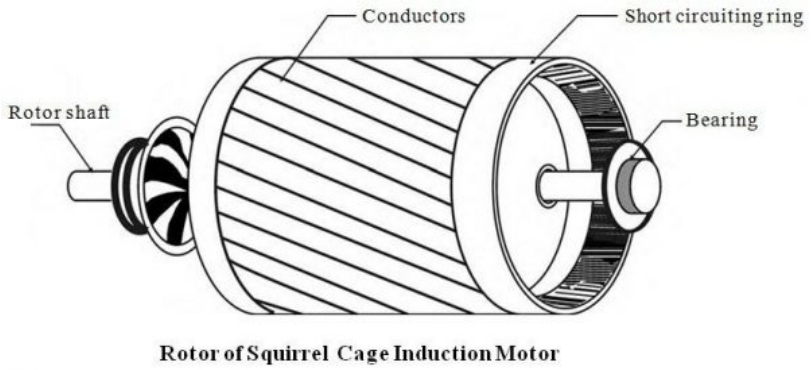

Figure 1.4: squirrel-cage type rotor[5]

1.2.2.2 Wound-rotor type induction motor

In this variant, rotor conductors exist as insulated windings that are not shorted by end rings. Instead, the terminals of these windings are brought out to connect to three insulated slip rings mounted on the shaft, as depicted in Fig. 1.5. Electrical connections to the rotor occur externally through brushes placed on the slip rings, hence earning this motor type the moniker "slip ring induction motor." Additionally, other components integral to the induction motor include:

(i) End flanges: Two end flanges support the bearings located at both ends of the motor.

(ii) Bearings: Two sets of bearings are positioned at each end of the rotor to support the rotating shaft.

(iii) Shaft: Constructed from steel, the shaft transmits generated torque to the load, facilitating mechanical power transfer.

(iv) Cooling fan: Located at the non-driving end of the motor, it provides forced cooling for both stator and rotor.

(v) Terminal box: Positioned on the outer cylindrical frame of the stator, it facilitates external electrical connections

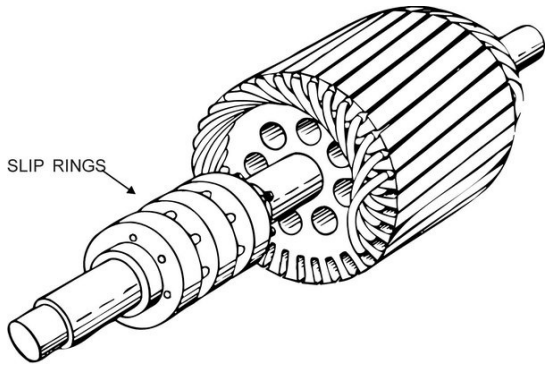

Figure 1.5: Slip ring rotor [5]

1.3 Principle of operation

When an induction motor's stator winding connects to a three-phase power supply, it generates a uniform rotating magnetic field [6]. This field induces an electromotive force (e.m.f.) in the rotor, which can rotate freely within the stator core with the assistance of ball bearings. As the rotor is short-circuited, either through end rings or external resistance, currents flow due to the induced e.m.f. These currents interact with the rotating magnetic field, creating torque on the rotor in the direction of the field. Since the rotor is free to rotate, this torque causes it to move in the direction of the stator field, enabling self-starting in a three-phase induction motor.

In the conversion of electrical energy to mechanical energy, induction motors experience various losses:

- Friction and windage losses (5–15%)
- Iron or core losses (15–25%)
- Stator losses (25–40%)

- Rotor losses (15–25%)
- Stray load losses (10–20%)

The full-load efficiency of a motor typically ranges from about 85% to 97% [7].

Induction motors offer simplicity, cost-effectiveness, and efficiency. Among them, squirrel-cage induction motors are particularly robust and efficient compared to wound-rotor induction motors. When supply voltage and frequency remain constant, a squirrel-cage induction motor runs at a consistent speed, making it suitable for constant-speed applications [1, 4]. Various standard designs of squirrel-cage induction motors are available in the market, categorized into classes A, B, C, and D, each tailored to meet the starting and running requirements of different industrial applications [8]. Table 1.1 provides a comparison of the different classes of squirrel-cage induction motors.

Table 1.1: Various classes of squirrel-cage induction motors [9]

	Class A	**Class B**	**Class C**	**Class D**
Properties	Normal starting torque, high starting current and low operating slip	Normal starting torque, low starting current and low operating slip	High starting torque and low starting current	High starting torque, low starting current and high operating slip
example of uses	Fan, pump load etc. where torque is low at start	For constant speed drive such as pump, blower	Compressor, conveyors, crushers etc.	For driving intermittent load, e.g. punch press.

1.4 Faults in induction motor

Induction motors are known for their ruggedness, affordability, low maintenance requirements, compact size, high efficiency, and compatibility with readily available power sources. Despite their reliability, they are susceptible to various undesirable faults. Through the examination of their construction and operation, it becomes evident that the most vulnerable components to faults in

induction motors include bearings, stator windings, rotor bars, and the shaft. Additionally, non-uniformity in the air gap between the stator's inner surface and the rotor's outer surface can also lead to faults.

Numerous studies have been conducted to analyze the reliability, performance, and occurrence of faults in motors [10, 11]. Statistical analyses by organizations like IEEE and EPRI have provided valuable insights into motor faults. For instance, IEEE Standard 493-1997 outlines the most common faults and their statistical occurrences, as shown in Table 1.3. Similarly, under EPRI sponsorship, General Electric Company conducted a study based on motor manufacturer reports, presenting the main motor faults in Table 1.2 [12, 13].

Table 1.2: Number of faults/failures by type and motor [9]

Type of faults	**Induction motor**	**Synchronous motor**	**Wound-rotor motor**	**DC motor**	**All total motors**
Bearing	152	2	10	2	166
Winding	75	16	6	-	97
Rotor	8	1	4	-	13
Shaft	19	8	-	-	19
slip ring	-	6	8	2	16
External device	10	7	1	-	18
Others	40	9	-	2	51

Table 1.3: Fault occurrence possibility on induction motor [12, 13]

Studied by	**Bearing fault (%)**	**Stator fault (%)**	**Rotor fault (%)**	**Others (%)**
IEEE	42	28	8	22
EPRI	41	36	9	14

Faults in induction motors can be broadly categorized into three types: (a) Electrical-related faults: These include unbalanced supply voltage or current, single phasing, under or overvoltage, reverse phase sequence, earth fault, overload, inter-turn short-circuit faults, and crawling. (b) Mechanical-related faults: This category encompasses broken rotor bars, mass unbalance, air gap

eccentricity, bearing damage, rotor winding failure, and stator winding failure. (c) Environmental-related faults: Factors such as ambient temperature and external moisture can impact motor performance. Additionally, machine vibrations due to installation defects or foundation issues can also affect performance [14]. The faults listed in Table 1.2 provide a broad overview, but it's important to recognize that faults in induction motors can manifest in various forms. To better identify these faults, they can be categorized as follows: (i) broken bar fault, (ii) rotor mass unbalance fault, (iii) bowed rotor fault, (iv) bearing fault, (v) stator winding fault, (vi) single phasing fault, and so on. Additionally, the phenomenon known as "crawling," where the motor fails to accelerate to its rated speed and instead operates at nearly one-seventh of its synchronous speed, is also considered a fault.In the subsequent sections, each of these fault types will be explored in detail, providing a comprehensive understanding of their causes and effects.

1.4.1 Broken rotor bar fault

1.4.1.1 General description of broken rotor bar

Broken rotor bar faults in induction motors occur when one or more rotor bars within the squirrel cage assembly are partially cracked or completely broken. This fault can lead to asymmetrical distribution of rotor currents and affects motor performance [15]. Figure 1.6 shows a broken rotor bar.

1.4.1.2 Causes of broken rotor bar

1. Manufacturing defects: Non-uniform metallurgical stresses during the brazing process or other manufacturing defects can weaken rotor bars, leading to failure during operation [16].

2. Centrifugal forces: Heavy end rings on the rotor can exert significant centrifugal forces, causing extra stress on the rotor bars and increasing the likelihood of damage.

3. Thermal and mechanical stresses: Thermal stresses from overheating or mechanical stresses resulting from bearing faults can weaken rotor bars and contribute to their failure.

4. Frequent starts and stops: Motors subjected to frequent starts and stops or long start-up times are more prone to rotor bar damage due to increased mechanical stress.

5. Fatigue: Over time, fatigue of the metal in the rotor bars can weaken them, making them susceptible to cracking and eventual failure.

The consequences of a broken rotor bar can be severe, as it can lead to higher currents flowing through adjacent bars, resulting in larger thermal and mechanical stresses [17]. Continued operation in this condition can cause additional bars to crack, leading to widespread damage within the rotor assembly. Cracks may occur at various locations, including within the bars, at the joints of bars and end rings, or in the end rings themselves, with a higher likelihood at the joints.

Identifying and addressing the causes of broken rotor bar faults is crucial for maintaining the performance and reliability of induction motors.

Figure 1.6: Broken rotor bar [18].

1.4.1.3 Effect of broken rotor bar

Cracked or broken bar fault produces a series of sideband frequencies [19, 20], in the stator current signature given by

$$f_{brb} = f\left(1 \pm 2ks\right) \tag{1.1}$$

where f is the supply frequency, s is the slip, and k is an integer. This has been demonstrated as a ripple effect in , which explains that the lower sideband at $f(1-2s)$ is the strongest, which will cause ripples of torque and speed at a frequency of $2sf$, and this in turn will induce an upper sideband at $f(1+2s)$. This effect will continue to create the above series of sidebands, i.e., $f(1\pm 2ks)$. The magnitude of this lower sideband $f(1-2s)$ over the fundamental can be used as an indicator of rotor broken bar fault [21].

1.4.2 Rotor mass unbalance

In understanding the construction of a motor, it becomes evident that the rotor sits within the stator bore and rotates coaxially with it. In a properly functioning motor, the rotor is centrally aligned with the stator, sharing the same axis of rotation. This alignment ensures uniform air gap between the rotor's outer surface and the stator's inner surface. However, if the rotor deviates from this central alignment or its axis differs from the geometrical axis of the stator, it results in what is known as air-gap eccentricity.

Air-gap eccentricity, a common fault in rotor assemblies of induction motors, can stem from various rotor faults such as rotor mass unbalance or bowed rotor. This fault leads to an imbalance in electromagnetic pull within the motor. The side of the rotor with the minimum air gap experiences greater pull, while the opposite side experiences lower pull. Consequently, the rotor tends to move in the direction of greater pull across the uneven gap [22]. The risk of rotor pullover is highest during motor startup when current flow is at its peak. In severe cases, rotor movement may lead to rubbing against the stator, potentially causing damage to both components [23].

1.4.2.1 General description of rotor mass unbalance

Rotor mass unbalance typically arises from manufacturing defects. However, it can also develop over time due to asymmetrical mass distribution around the rotor's center of rotation, internal misalignment, or shaft bending. These factors cause the rotor's center of gravity to deviate from its center of rotation. In cases of severe rotor eccentricity, unbalanced electromagnetic forces may cause the rotor to make contact with the stator, resulting in the removal of material from the rotor

body. This phenomenon, referred to as mass subtraction, exacerbates rotor mass unbalance.

1.4.2.2 Classification of mass unbalance

In the realm of mass unbalance classification, there exist three distinct types:

1. Static mass unbalanced rotor
2. Couple unbalanced rotor
3. Dynamic unbalanced rotor

1.4.2.3 Static mass unbalanced rotor

In this scenario, the shaft's rotational axis and the weight distribution axis of the rotor run parallel but are offset, as depicted in Figure 1.7. Detecting this type of eccentricity without specialized equipment poses significant challenges [24].

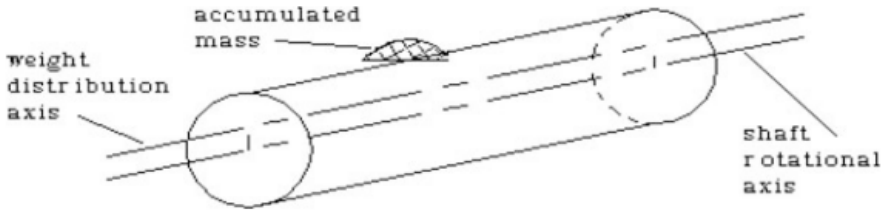

Figure 1.7: static mass unbalanced rotor [5]

1.4.2.4 Couple unbalanced rotor

As illustrated in Figure 1.8, this fault manifests when the shaft's rotational axis and the weight distribution axis of the rotor intersect at the center of the rotor.

1.4.2.5 Dynamic unbalanced rotor

In the domain of rotor mass unbalance, the category of Dynamic Unbalanced Rotor is delineated. When this fault emerges, the shaft's rotational axis and the weight distribution axis of the

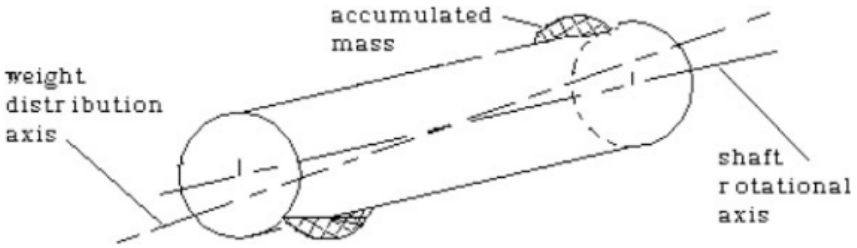

Figure 1.8: couple unbalanced rotor [5]

rotor fail to coincide, as depicted in Figure 1.9. Dynamic unbalance represents a combination of coupling unbalance and static unbalance.

The principal causes of rotor mass unbalance in an induction motor can be itemized as follows:

- Manufacturing defects
- Internal misalignment or shaft bending
- Occurrence over time, due to nonsymmetrical addition or subtraction of mass around the rotor's center of rotation.

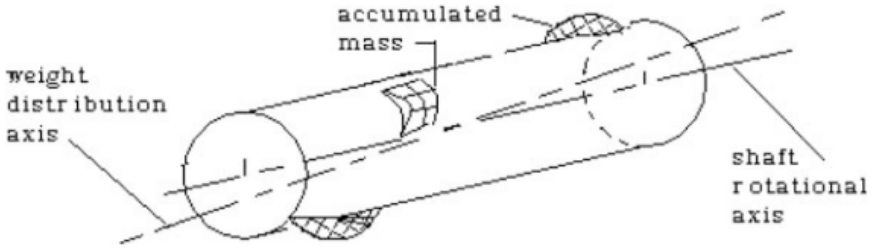

Figure 1.9: Dynamic unbalanced rotor[5]

1.4.2.6 Effect of rotor mass unbalance

In the event of rotor mass unbalance in an induction motor, the resulting effects are outlined as follows:

- The occurrence of mass unbalance triggers dynamic eccentricity, leading to oscillations in the length of the air gap.

- These oscillations in the air gap length induce variations in the density of the air gap flux, subsequently causing fluctuations in the induced voltage across the winding.

Furthermore, the induced voltage generates currents whose frequencies are dictated by the frequency of the harmonics in the air gap flux density. The formula for stator current harmonics [25, 26] is expressed as:

$$f_{brb} = f\left(1 \pm 2ks\right) \tag{1.2}$$

Here, f denotes the supply frequency, s represents the slip of the motor, p signifies the number of pole pairs, and k is an integer.

1.4.3 Bearing fault

The rotor of an induction motor is supported by two sets of bearings positioned at both ends. These bearings support the rotor, enabling it to rotate with minimal friction. Each bearing assembly comprises inner and outer rings, referred to as races, with a series of rolling elements, typically balls, situated between them. In the motor setup, the inner race is typically affixed to the shaft, transmitting the load through the rotating balls, thereby reducing friction. Additionally, the application of lubricants such as oil or grease between the races further diminishes friction. Figure 1.10 showcases a cross-sectional view of a ball bearing assembly.

Any form of physical damage incurred by the inner or outer races or the surface of the balls is categorized as a bearing fault. Within the context of induction motor failures, bearings represent the most vulnerable component. Bearing faults are recognized as the primary cause of failures in induction motors, constituting the largest proportion of faults. According to studies conducted by IEEE and EPRI, as detailed in Table 1.3, approximately 41–42% of faults in induction motors stem from bearing failures [12, 13].

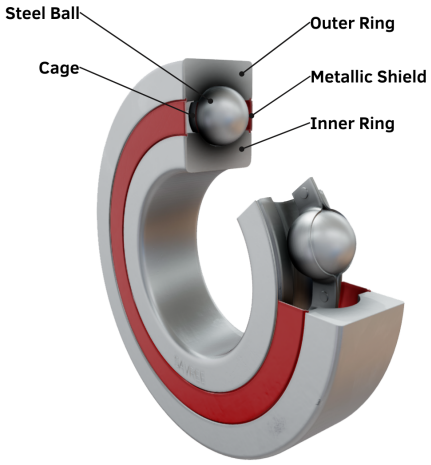

Figure 1.10: Ball bearing [27]

1.4.3.1 Causes and effects of bearing failure

1. **Excessive loads, tight fits, and excessive temperature rise**: These factors can lead to the annealing of the two races and ball materials, as well as degradation or destruction of the lubricant. When the load surpasses the elastic limit of the bearing material, brinelling, a form of surface damage, occurs.

2. **Fatigue failure**: Prolonged operation of the bearings can cause fatigue failure, resulting in fractures and the removal of small particles from the surfaces of races or balls. This type of bearing failure is progressive and can lead to increased vibration and noise levels in the motor [28].

3. **Corrosion**: Exposure to corrosive fluids or atmospheres can result in the corrosion of bearings. Corrosion may also occur if lubricants deteriorate or if bearings are carelessly handled during installation [28]. Early fatigue failure may occur as a result of corrosion.

4. **Contamination**: Contamination by dirt and foreign particles, common in industrial environments, is a major cause of bearing failure. Contaminated lubricants lead to increased vibration and wear.

5. **Lubricant failure**: Restricted flow of lubricant or excessive temperatures can cause lubricant failure. This degradation of lubricant properties leads to excessive wear of balls and races,

resulting in overheating. Melting and leakage of grease lubricant indicate lubricant failure.

6. **Misalignment of bearings**: Misalignment leads to wear on the surfaces of balls and races, resulting in increased bearing temperature.

In the event of bearing failure, friction typically increases, leading to elevated bearing temperatures and increased machine vibration. Monitoring bearing temperature and vibration can provide valuable insights into bearing condition and overall machine health [28, 29].

1.4.4 Stator fault

The stator of an induction motor is exposed to various stresses [30], including mechanical, electrical, thermal, and environmental factors [22]. Proper operation and maintenance can help manage these stresses effectively. Stator faults can typically be classified into two categories: faults in the laminations and frame of the stator, and faults in the stator winding. Among these, faults in the stator winding are the most common. According to research conducted by IEEE and EPRI, given in Table 1.3 approximately 28-36% of induction motor faults are attributed to stator winding faults [12, 13]. Many of these faults result from a combination of the aforementioned stresses.

1.4.4.1 Stator winding fault

Stator winding faults typically result from insulation failure within the stator winding, often referred to as inter-turn short-circuit faults. Various types of stator winding faults include:

1. Turn-to-turn fault: Short circuit between two turns of the same phase.
2. Coil-to-coil fault: Short circuit between two coils of the same phase.
3. Phase-to-phase fault: Short circuit between turns of two different phases.
4. Short circuit between turns of all three phases.
5. Coil-to-ground fault: Short circuit between winding conductors and the stator core.

6. Open-circuit fault: Occurs when the winding breaks, resulting in a discontinuity in the flow of current.

Different types of stator winding faults are illustrated in Figure 1.11. Short-circuit faults occur when a total or partial portion of the stator windings becomes shorted, while open-circuit faults occur when a total or partial portion of the stator windings becomes disconnected, resulting in the absence of current flow in that phase/line (refer to Figure 1.12).

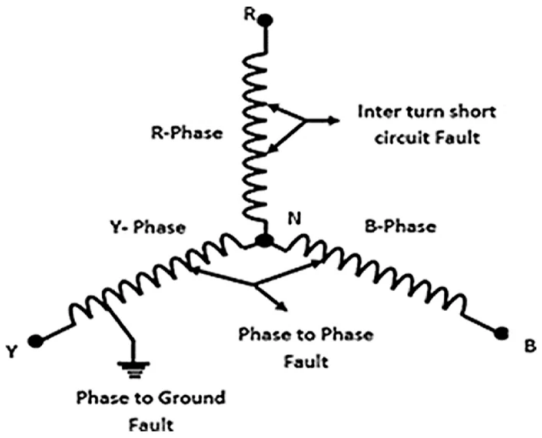

Figure 1.11: Star-connected stator showing different types of stator winding fault [5]

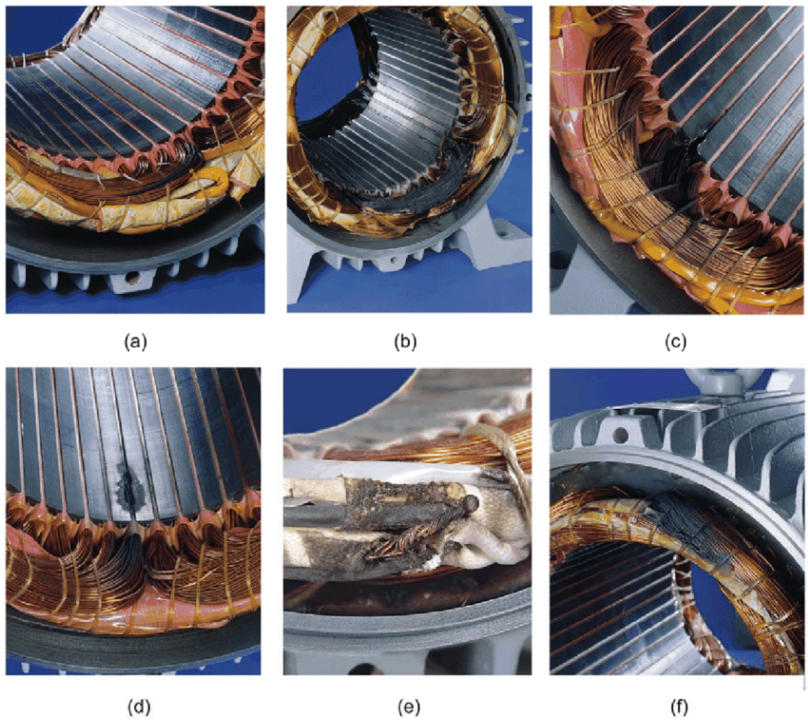

Figure 1.12: Typical insulation damage leading to inter-turn short circuit of the stator windings in three-phase induction motors. **(a)** Inter-turn short circuits between turns of the same phase. **(b)** Winding short circuited. **(c)** Short circuits between winding and stator core at the end of the stator slot. **(d)** Short circuits between winding and stator core in the middle of the stator slot. **(e)** Short circuit at the leads. **(f)** Short circuit between phases. [5]

1.4.4.2 Causes and effects of stator winding faults

1. **Mechanical stresses:** Mechanical stresses occur due to the movement of the stator coil and rotor impacting the stator[30]. Coil movement induced by stator current, which increases with the square of the current, may loosen top sticks and damage copper conductors and insulation [31]. Rotor striking the stator, caused by misalignment, shaft deflection, or bearing failure, can puncture coil insulation, leading to coil-to-ground faults. High mechanical vibration may also disconnect the stator winding, resulting in open-circuit faults [32].

2. **Electrical stresses**: Electrical stresses primarily result from supply voltage transients caused by faults (line-to-line, line-to-ground, or three-phase), lightning, circuit breaker operations,

or variable frequency drives [30]. These transients reduce the life of stator windings and can cause turn-to-turn or turn-to-ground faults.

3. **Thermal stresses:** Thermal stresses stem from thermal overloading and are a major cause of insulation deterioration in stator windings. They occur due to sustained overload or fault currents, high ambient temperatures, inadequate ventilation, or unbalanced supply voltages [30]. A general guideline suggests that winding temperature increases by 25% in the phase with the highest current for every 3.5% voltage unbalance per phase [22]. Rapid motor starts and stops also elevate winding temperature. Exceeding the motor's temperature limit can lead to rapid insulation failure. Additionally, for every 10°C increase above the stator winding temperature limit, insulation life is halved. Table 1.4 illustrates the impact of temperature rise above ambient on winding insulation [22].

4. **Environmental stresses:** These stresses may arise when the motor operates in an unfavorable environment, characterized by excessive heat, cold, or humidity. The presence of foreign materials can contaminate the insulation of the stator winding and hinder heat dissipation from the motor[33], thereby reducing the insulation life. Adequate airflow is crucial in the motor's vicinity to prevent the accumulation of heat. Otherwise, elevated temperatures in the rotor and stator will decrease insulation life..

Table 1.4: Effect of Rise of Temperature on Insulation Life [22]

Ambient Temperature (°C)	**Insulation Life (hours)**
30	250,000
40	125,000
50	60,000
60	30,000

1.4.5 Single phasing fault

1.4.5.1 Causes of single phasing fault

Single phasing faults in an induction motor may be caused by:

- Power outage or blown fuse in the utility system.
- Equipment failure in the supply system.
- Short circuit in one phase of the star-connected or delta-connected motor.

1.4.5.2 Effects of single phasing fault

The effects of single phasing faults include:

- Overheating of motor windings due to the flow of negative sequence current.
- Continued operation of the motor during single phasing fault, relying on torque from the remaining two phases, which can overload and overheat healthy phases, leading to critical motor damage.
- Inability of a three-phase motor to start if a single phasing fault persists in the supply line.

1.4.6 Condition monitoring and its necessity

Induction motors are pivotal in industrial operations due to their durability, cost-effectiveness, low maintenance, compact size, reasonable efficiency, and compatibility with readily available power supplies. Approximately half of a nation's total generated power is consumed by these induction motors, underscoring their widespread use. However, they have operational limitations, and exceeding these conditions may lead to premature stator or rotor failures. Such failures can halt entire industrial processes, resulting in lost production time and financial losses. Therefore, preventing induction motor failures is crucial[34].

Operators and technicians face continuous pressure to prevent unscheduled downtime and reduce maintenance costs. Maintenance of electrical motors can take various forms: breakdown maintenance, fixed-time maintenance, and condition-based maintenance. Breakdown maintenance entails

running the motor until it fails, leading to costly replacements and productivity losses. Fixed-time maintenance involves scheduled motor stops for inspection, resulting in prolonged downtime and requiring skilled technicians for fault recognition. Hence, condition-based maintenance, where actions are taken at the first signs of an impending fault, is preferred [34, 35].

In condition monitoring, signals from the motor are continuously monitored to assess its health during operation, enabling the early detection of faults. This approach, also known as online condition monitoring, allows for preventive maintenance planning and spare parts arrangement, optimizing maintenance schedules and minimizing motor downtime [13]. The benefits of condition monitoring include the prediction of motor failure, optimization of motor maintenance, reduction of maintenance costs, minimization of machine downtime, and improvement of motor reliability.

1.5 Conclusion

This chapter provides an introductory overview of induction motors, detailing their construction, operation, and common faults. It underscores the importance of induction motors in various applications and discusses essential components like the stator and rotor. The operational principles are explained, focusing on the interaction between the stator and rotor to generate motion. The chapter identifies various types of faults in induction motors, such as broken rotor bars, rotor mass unbalance, bearing faults, stator faults and single phasing. Each fault is described with its causes and effects, highlighting the necessity of proactive maintenance and condition monitoring to prevent downtime. Overall, Chapter 1 sets the foundation for subsequent chapters on fault detection and diagnosis techniques.

Chapter 2

The state of the art: Bearing fault diagnosis methods

2.1 Introduction

Bearing fault diagnosis in induction motors is critical due to its significant impact on operational reliability and maintenance efficiency, with approximately 40% to 50% of motor failures attributed to bearing faults [36]. These failures lead to unplanned downtime and substantial costs related to repairs, replacements, and production losses. Traditional diagnostic methods like visual inspection and manual monitoring are often insensitive and unreliable for detecting early-stage bearing faults and are labor-intensive and time-consuming, making them unsuitable for real-time industrial monitoring. Consequently, there is increasing interest in advanced diagnostic approaches that offer improved accuracy, efficiency, and predictive capabilities. Besides signal-based and Artificial intelligence (AI)-based methods, model-based and statistical approaches are also used for bearing fault diagnosis. Model-based methods develop mathematical models to simulate motor behavior under normal and faulty conditions, while statistical approaches analyze motor performance metrics to identify abnormal patterns. Based on a survey of previous works [37], it has been shown that most approaches to bearing fault diagnosis are signal-based and AI-based methods. This thesis focuses on combining these two approaches, presenting new and promising results.This chapter explores the principles, methodologies, applications, and comparative analyses of these approaches, highlighting their strengths, limitations, and potential synergies.

2.2 Signal-based approaches

Signal-based approaches in bearing fault diagnosis involve the analysis of various physical signals produced by the induction motor during operation. These signals carry valuable information about the mechanical condition of the motor components, including bearings. By extracting and analyzing relevant features from these signals, it is possible to detect early signs of bearing faults and assess the severity of degradation.The main signals used in these approaches include vibration, acoustic emission, and current.

Signal processing methods have evolved over time, with research categorized into three stages: Stage I (pre-2001), Stage II (2001–2010), and Stage III (2011 onwards). Early work in Stage I

focused on simple statistical parameters such as kurtosis and root mean square value. However, these methods were limited in their ability to mitigate noise and interferences from other sources of vibration. In Stage II, frequency-based methods such as FFT analysis, high-frequency resonance technique (HFRT), envelope analysis, and power spectral density became common for diagnosing rolling element bearings. Stage III introduced time-frequency domain analysis methods, including short-time Fourier transform (STFT), wavelet transform, and Hilbert-Huang transform, which offered enhanced capabilities for bearing fault diagnosis [38].The following section provides a detailed description of each stage.

2.2.1 Time domain analysis techniques

Time domain analysis technique is the simplest used technique for bearing defect detection. The process, in which some characteristics features as well as statistical parameters are computed from the signal data, is known as time domain analysis, where the Time-domain is the graph of the signal amplitude versus time. In time waveform analysis, the defects are detected with the help of some statistical parameters like Peak, Peak-to-peak, Root means square (RMS), Crest factor, Skewness, Kurtosis, Clearance factor, Impulse factor, Shape factor, etc. The most commonly used statistical parameters for bearing defect detection are Peak, RMS, Crest factor, Skewness, and Kurtosis [38].

- **Peak-to-peak value:** This represents the difference between the maximum and minimum amplitude values in the signal. It provides insight into the overall variation of the signal. Let X_i represent the amplitude values of the signal at different points in time. The equation is given by:

$$\text{Peak-to-Peak Value} = \max(X_i) - \min(X_i) \tag{2.1}$$

- **RMS value (root mean square):** This is the square root of the average of the squared values of the signal [39]. It represents the effective amplitude of the signal and is useful for understanding the signal's energy content.its equation is given by:

$$\text{RMS} = \sqrt{\frac{1}{N}\sum_{i=1}^{N} x_i^2} \tag{2.2}$$

N is the number of separate point and refers to the signal from each sampled point

- **The crest factor:** This is the ratio of the peak value to the RMS value of the signal. It indicates the peakiness of the signal and can help identify transient events or peaks in the signal [39].it is given by:

$$\text{Crest factor} = \frac{\text{Peak}}{\text{RMS}} \tag{2.3}$$

- **Skewness:** Skewness measures the asymmetry of the signal's amplitude distribution. A positive skewness indicates a longer tail on the right side of the distribution, while a negative skewness indicates a longer tail on the left side.it is given by:

$$\text{Skewness} = \frac{\sum_{i=1}^{N}(x_i - \text{Mean})^3}{N \cdot \text{Standard deviation}^3} \tag{2.4}$$

- **Kurtosis:** Kurtosis measures the "tailedness" or peakedness of the signal's distribution. It indicates whether the distribution is heavy-tailed or light-tailed compared to a normal distribution. High kurtosis implies heavy tails and a sharper peak, while low kurtosis indicates lighter tails and a flatter peak [39].it is given by:

$$\text{Kurtosis} = \frac{\sum_{i=1}^{N}(x_i - \text{Mean})^4}{N \cdot \text{Standard deviation}^4} \tag{2.5}$$

2.2.2 Frequency domain analysis techniques

Frequency domain analysis (FDA) or spectral analysis is a widely used method for detecting defects in rotating equipment bearings (REBs). This approach involves analyzing signals in the frequency domain, where the signal's amplitude is represented as a function of frequency rather than time [40]. FDA techniques, including spectrum analysis and envelope analysis, are employed to

identify specific frequency components indicative of defects or anomalies in REBs. By decomposing signals into their constituent frequency components, technicians can pinpoint frequencies associated with common types of bearing defects, such as inner race, outer race, or rolling element faults. This allows for early detection of defects and differentiation between fault types, enabling proactive maintenance and minimizing unplanned downtime in industrial machinery.

2.2.2.1 Spectrum analysis:

Spectrum analysis is a fundamental technique used in the analysis of signals to uncover valuable insights about their frequency components. It involves converting time-domain signals into frequency-domain signals using Fourier transform. This transformation allows for the visualization of the frequency spectrum, which graphically depicts the relationship between signal amplitude and frequency [38]. The amplitude of the signal can be measured in terms of displacement, velocity, or acceleration, providing valuable information about the behavior of the signal.

a) Power Spectrum:

The power spectrum, derived from the Fourier transform of a time-domain signal, serves as a valuable tool for signal analysis. It quantifies the distribution of signal power across different frequencies, providing a comprehensive understanding of signal characteristics. Mathematically, the power spectrum $P(f)$ can be expressed as the square of the magnitude of the Fourier transform $X(f)$ of the signal [41]. This relationship is represented by the equation:

$$P(f) = |X(f)|^2 = X(f)X^*(f) \tag{2.6}$$

Where: $X(f)$ is the Fourier transform of the signal in the frequency domain. $X^*(f)$ denotes the complex conjugate of $X(f)$. $P(f)$ represents the power spectrum, indicating the power distribution across different frequencies.

b) Fast fourier transform (FFT): A key tool in spectrum analysis is the Fast fourier transform (FFT), which efficiently computes the discrete Fourier transform of a signal. The FFT algorithm significantly speeds up the computation process, making it practical for real-time analysis of signals [42]. The FFT is given by:

$$X[k] = \sum_{n=0}^{N-1} x[n] e^{-j2\pi \frac{kn}{N}} \tag{2.7}$$

Where:

- $X[k]$ represents the DFT of the signal in the frequency domain.
- $x[n]$ is the discrete signal being analyzed.
- k denotes the frequency bin at which the signal is being analyzed.
- N is the total number of samples in the signal.

However, it's essential to note that while FFT is effective for analyzing periodic stationary signals, it may lose time information when applied to non-stationary signals. This limitation should be considered when interpreting the results of FFT analysis in practical applications. Nonetheless, FFT remains a powerful tool for extracting frequency information from signals and identifying defects in bearing rolling elements, providing valuable insights into their severity, location, and nature.

2.2.2.2 Envelope analysis:

Envelope analysis (EA), also referred to as "amplitude demodulation," "demodulated resonance analysis," "high-frequency resonance Technique (HFRT)," and "narrow band envelope analysis," presents an alternative approach to detecting bearing defects. Bearings afflicted with defects often produce repetitive signal patterns characterized by lower amplitudes and higher frequencies compared to other signals. Envelope analysis aims to isolate these repetitive frequency components occurring within the defect frequency range by removing low-frequency stationary components from the signal [38].

This process of enveloping enhances the visibility of defect-related frequencies, facilitating their identification amidst the noise of the overall signal. By separating the defect frequencies from the natural frequencies of the rotating parts through demodulation, envelope analysis enables targeted analysis of the defect-induced signal variations.

The demodulation process employed in envelope analysis helps distinguish between the underlying defect-related signals and the broader spectrum of signals present in machinery operations. Figure 2.1 illustrates the steps involved in envelope analysis, providing a visual representation of the process for enhanced understanding and implementation.

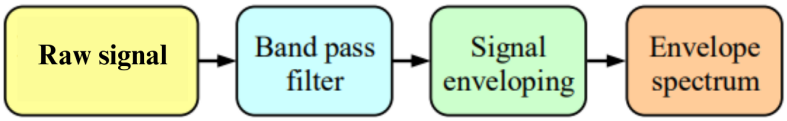

Figure 2.1: Process of envelop analysis [43]

2.2.3 Time-frequency domain analysis techniques:

Time-frequency domain analysis (TFDA), also known as spectrogram analysis, provides a comprehensive approach for analyzing signals, accommodating both stationary and non-stationary characteristics [44]. TFDA involves simultaneous analysis of vibration signals in both time and frequency domains, enabling the capture of evolving spectrum components over time. A variety of TFDA techniques have been developed to address challenges posed by high noise levels and numerous frequency components in rotating machinery. These techniques include short time fourier transform (STFT), wavelet transform (WT), wigner-ville distribution (WVD), hilbert huang transform (HHT), and local mean decomposition, among others. Among these methods, WT stands out as particularly popular and effective for defect detection and diagnosis.In the following subsection, there will be further description of main techniques and algorithms.

2.2.3.1 Short time fourier transform (STFT):

The short time fourier transform (STFT), introduced by Dennis Gabor in 1946, is a crucial technique for analyzing non-stationary signals. It breaks down these signals into small time segments, calculating the spectrum of each segment through fast fourier transform (FFT), also known as windowing the signal. STFT offers insights into signal changes over time and frequency. Although it provides a valuable representation of signals in both domains, it faces limitations in balancing frequency and time domain resolutions [45].

The mathematical representation of the short-time fourier transform (STFT) is as follows:

$$\text{STFT}(\tau, f) = \int_{-\infty}^{\infty} x(t) \cdot w(t - \tau) \cdot e^{-j2\pi ft}\, dt \tag{2.8}$$

Where:

- $\text{STFT}(\tau, f)$ represents the STFT of the signal at time τ and frequency f.
- $x(t)$ is the original time-domain signal.
- $w(t - \tau)$ is the window function centered at time τ.
- $e^{-j2\pi ft}$ is the complex exponential representing the frequency modulation.

However, STFT has shown promise in various applications. For instance, Cocconcelli et al. [77] utilized STFT for defect detection in ball bearings, enhancing fault features through time-frequency averaging. Similarly, Gao et al. [78] applied STFT to describe localized faults in rotating equipment bearings (REB) and addressed FFT's limitations in handling non-stationary signals. Figure 2.2 illustrate short time fourier transform map.

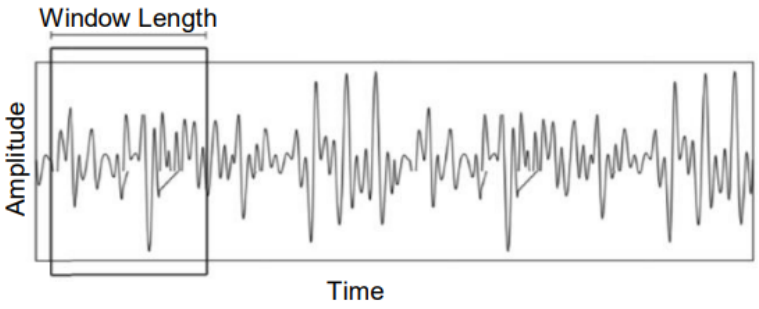

Figure 2.2: short time fourier transform illustration [43]

2.2.3.2 Wavelet transform (WT):

The wavelet transform (WT) emerges as a vital tool for analyzing non-stationary signals in various domains, gaining traction due to its robust performance in time and frequency domain analysis. Introduced by mathematician Morlet in 1984, WT characterizes signals by correlating

them with translations and dilations of a mother wavelet function. Compared to the short time fourier transform (STFT), WT offers superior frequency resolutions with sharper time resolutions. Notably, the continuous wavelet transform (CWT), discrete wavelet transform (DWT), and wavelet packet transform (WPT) are widely utilized variants [45].

CWT decomposes signals into time and frequency components using a mother wavelet, mathematically expressed as:

$$CWT(a,b) = \int_{-\infty}^{\infty} x(t) \cdot \psi^* \left(\frac{t-b}{a} \right) dt \cdot a^{-1} \tag{2.9}$$

Here, $\psi^*(t)$ denotes the complex conjugate of the mother wavelet, a signifies the scale parameter (inverse of frequency), and b indicates time-shifting or translation.

DWT, derived from discretizing CWT, reduces computational load by adopting dyadic scales and translations:

$$DWT(j,k) = \int_{-\infty}^{\infty} x(t) \cdot \psi_{j,k}^*(t)\, dt \cdot 2^{j/2} \tag{2.10}$$

Here, j and k are integers, representing scale and translation parameters, respectively, and $\psi_{j,k}^*(t)$ is the complex conjugate of the wavelet function.

WPT, an advanced variant, employs multiple filters to further decompose signals, particularly beneficial for detecting transient components with high-frequency attributes. The WT's adaptability and capability to furnish both time and frequency domain representations position indispensable tool for signal analysis in various fields, evidenced by its growing adoption across diverse applications.

2.2.3.3 Variational mode decomposition (VMD):

Variational mode decomposition VMD decompose the given signal into a collection of subsignals called Intrinsic Mode Functions (IMFs) by solving a contrained variationnal problem, where each IMF is regarded as an amplitude-modulated and frequency modulated (AM-FM) signal. It has band-limited and around a center pulsation. The constrained variational problem is formulated as follows [46]:

$$\begin{aligned} &\min_{\{u_k\},\{\omega_k\}} \left\{ \sum_{k=1}^{K} \left\| \frac{\partial}{\partial t} \left[\left(\delta(t) + \frac{j}{\pi t} \right) u_k(t) \right] e^{-j\omega_k t} \right\|_2^2 \right\} \\ &\text{s.t.} \quad \sum_{k=1}^{K} u_k = f(t) \end{aligned} \tag{2.11}$$

Where k stands for each mode, $k \in \{1, 2, \ldots, K\}$.

To solve the constrained variational problem, the augmented Lagrangian is introduced and the non-constrained variational problem is gotten by:

$$\begin{aligned} L(\{u_k\}, \{\omega_k\}, \{\lambda\}) = \alpha &\sum_{k=1}^{K} \left\| \frac{\partial}{\partial t} \left[\left(\delta(t) + \frac{j}{\pi t} \right) u_k(t) \right] e^{-j\omega_k t} \right\|_2^2 \\ &+ \left\| f(t) - \sum_{k=1}^{K} u_k(t) \right\|_2^2 \\ &+ \left\langle \lambda(t), f(t) - \sum_{k=1}^{K} u_k(t) \right\rangle \end{aligned} \tag{2.12}$$

Let α be the balancing parameter of the data-fidelity constraint, and $\lambda(t)$ be the Lagrange multipliers.

The iterative formulas of u_k and ω_k are deduced with the alternate direction method of multipliers (ADMM) as follows:

$$\hat{u}_k^{(n+1)}(\omega) = \frac{\hat{f}(\omega) - \sum_{i=1}^{k-1} \hat{u}_i^{(n+1)}(\omega) - \sum_{i=k+1}^{K} \hat{u}_i^{(n)}(\omega) + \hat{\lambda}_i(\omega)/2}{1 + 2\alpha(\omega - \omega_k^n)^2} \tag{2.13}$$

$$\omega_k^{(n+1)} = \frac{\int_0^\infty \omega \left| \hat{u}_k^{(n+1)}(\omega) \right|^2 d\omega}{\int_0^\infty \left| \hat{u}_k^{(n+1)}(\omega) \right|^2 d\omega} \tag{2.14}$$

- **Step 1:** Initialize $\hat{u}_k^{(1)}$, $\omega_k^{(1)}$, $\lambda_k^{(1)}$, and maximum iterative time N.
- **Step 2:** Update $\hat{u}_k(\omega)$ and ω_k according to Eq. (2.13) and Eq. (2.14):
- **Step 3:** Update λ based on Eq. (2.15).

$$\hat{\lambda}_k^{(n+1)}(\omega) = \hat{\lambda}_k^{(n)}(\omega) + \tau \left(\hat{f}(\omega) - \sum_{i=1}^{K} \hat{u}_i^{(n+1)}(\omega) \right) \tag{2.15}$$

until convergence:

$$\frac{1}{2} \left(\left\| \hat{u}^{(n+1)} - \hat{u}^{(n)} \right\|^2 + \left\| \omega^{(n+1)} - \omega^{(n)} \right\|^2 \right) < \varepsilon \tag{2.16}$$

In summary, VMD offers a data-driven approach to decompose signals into sparse and coherent oscillatory modes. By balancing data fidelity and sparsity regularization, VMD enables accurate extraction of fault signatures from non-stationary signals, providing valuable insights for bearing fault detection and diagnosis.

2.3 Artificial intelligence (AI) -based approaches

Traditional methods of fault detection often rely on manual inspection or signal analysis, which can be time-consuming and prone to human error. In recent years, the advent of artificial intelligence (AI) has revolutionized the field of predictive maintenance by offering automated and accurate fault detection techniques. AI-based approaches involve the use of algorithms and models to automatically learn patterns and relationships from data without being explicitly programmed. In the context of bearing fault diagnosis, these approaches aim to identify characteristic features indicative of faults and classify them accurately.

Machine learning is a subset of artificial intelligence that focuses on developing algorithms capable of learning from and making predictions or decisions based on data. Deep learning is a branch of machine learning that utilizes neural networks with multiple layers to extract hierarchical representations of data [47].The following subsections will discuss and focus on four powerful algorithms: Artificial neural networks (ANN), convolutional neural networks (CNN), multi-channel CNNs, and long short-term memory (LSTM) networks.

2.3.1 Artificial neural networks (ANNs)

Neural networks (ANNs) utilize a learning process that involves forward and backward propagation to train the network's parameters. This process, along with related components, can be summarized as follows:

1. **Forward propagation**:

   - During forward propagation, input data is fed into the network, and activations are computed sequentially through each layer until the output layer is reached as shown in the figure 2.4. This involves calculating the weighted sum of inputs to each node and applying the activation function to produce the node's output.
   - Forward propagation equations:

$$z_j = \sum_{i=1}^{n} w_{ij} x_i + b_j \tag{2.17}$$

$$a_j = \phi(z_j) \tag{2.18}$$

where:

- z_j is the weighted sum of inputs for the j-th neuron.
- w_{ij} is the weight between the i-th input and the j-th neuron.
- x_i is the i-th input to the neuron.
- b_j is the bias term for the j-th neuron.
- a_j is the activation of the j-th neuron.
- $\phi(z_j)$ is the activation function applied to z_j.

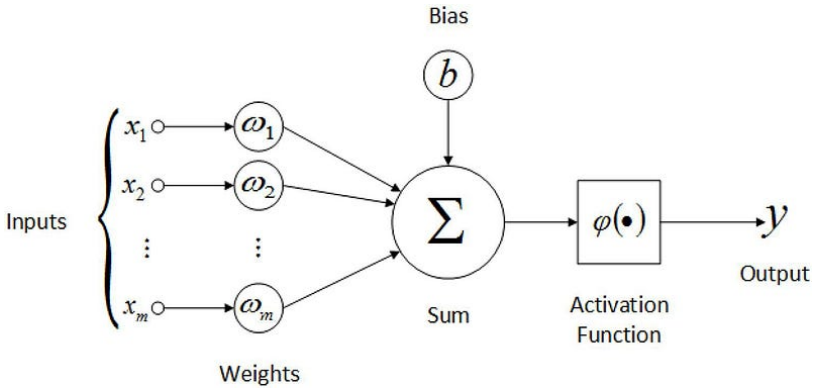

Figure 2.3: artificial perceptron feed forward [48]

2. **Activation functions**:

- The most commonly used activation function in the hidden layers is the Rectified Linear Unit (ReLU), defined as:

$$\phi(z) = \max(0, z) \tag{2.19}$$

- For the output layer, the choice of activation function depends on the nature of the problem.
  - For binary classification problems, the Sigmoid function is often used:

$$\phi(z) = \frac{1}{1 + e^{-z}} \tag{2.20}$$

– For multi-class classification problems, the Softmax function is frequently employed:

$$\phi(z_j) = \frac{e^{z_j}}{\sum_{k=1}^{K} e^{z_k}} \tag{2.21}$$

Where K represents the number of classes.

3. **Error function**:

   - The error function, also known as the loss or cost function, quantifies the discrepancy between the predicted output and the actual target values. The objective is to minimize this function.
   - Common error functions include:
     - Mean Squared Error (MSE) for regression:

$$E = \frac{1}{N}\sum_{i=1}^{N}(y_i - \hat{y}_i)^2 \tag{2.22}$$

     - Cross-Entropy Loss for classification:

$$E = -\frac{1}{N}\sum_{i=1}^{N}\sum_{k=1}^{K} y_{ik}\log(\hat{y}_{ik}) \tag{2.23}$$

4. **Backward propagation**:

   - After forward propagation, the error is propagated backward through the network to update the weights and biases. This involves computing the gradient of the error function with respect to each parameter in the network using techniques like the chain rule.
   - Backward propagation updates the parameters to minimize the error function using gradient descent:

$$W_{t+1} = W_t - \eta\nabla E \tag{2.24}$$

     Where W represents the parameters, η is the learning rate, and ∇E is the gradient of the error function.

5. **Optimizer**:

   - The optimizer updates the network parameters based on the computed gradients during backward propagation. Stochastic Gradient Descent (SGD) is a commonly used optimizer.

2.3.2 Convolutional neural networks (CNNs):

Convolutional neural networks (CNNs) are a class of deep learning models specifically designed for processing structured grid data such as images. CNNs are composed of multiple layers, including convolutional layers, pooling layers, and fully connected layers [47].

1. **Convolutional layer**:

   - In the convolutional layer, convolutional operations are performed on the input data using learnable filters or kernels. The output feature maps capture spatial hierarchies of patterns present in the input data.
   - The output feature map C is computed as:

$$C_{i,j} = \phi\left(\sum_m \sum_n I_{i+m,j+n} \cdot K_{m,n} + b\right) \tag{2.25}$$

     Where I is the input data, K is the kernel, b is the bias, and ϕ is the activation function.

2. **Pooling layer**:

   - The pooling layer downsamples the feature maps obtained from the convolutional layers, reducing their spatial dimensions while retaining the most important information.
   - Common pooling operations include max pooling and average pooling.

3. **Fully connected layer**:

   - The fully connected layer connects every neuron in one layer to every neuron in the next layer, allowing for high-level feature learning and classification.
   - The output of the fully connected layer is computed similarly to ANNs eq (2.17) and (2.18).

CNNs also involve a learning process similar to ANNs, including forward and backward propagation, error functions, and optimizers. The key difference lies in the structure and operations

performed within each layer, which are specifically tailored for processing grid-like data such as images,as depicted in Figure 2.5.

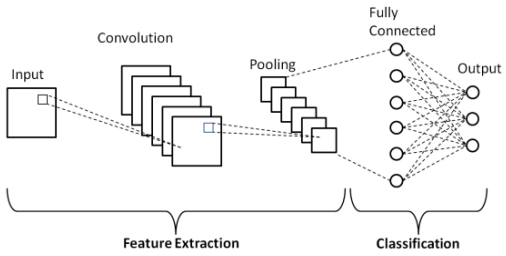

Figure 2.4: Convolutional neural networks architecture [49]

In the context of image classification, CNNs have shown remarkable performance, surpassing traditional computer vision methods in tasks such as object recognition and detection.

2.3.3 Multi-kernel size convolutional neural networks (CNNs):

Multi-kernel size convolutional neural networks (CNNs) are a variant of deep learning models tailored for structured grid data like images. They extend the traditional CNN architecture by incorporating filters of different sizes to capture features at various scales.

1. **Architecture**:

   - Multi-kernel size CNNs typically include multiple convolutional layers followed by pooling and fully connected layers. Each convolutional layer utilizes filters of different sizes to extract features across multiple spatial scales.

2. **Convolutional layer**:

   - The convolutional layer applies convolutional operations using filters of varying sizes to generate feature maps capturing diverse spatial patterns.

3. **Pooling layer**:

   - Pooling layers reduce the spatial dimensions of feature maps while preserving important information, similar to standard CNNs.

4. **Learning process**:

   - Multi-kernel size CNNs undergo a learning process involving forward and backward propagation, error computation, and optimization techniques, analogous to traditional CNNs.

Multi-kernel size CNNs offer advantages over standard CNNs by leveraging filters of different sizes, allowing for better extraction of features at various spatial scales without repeating details already covered in the CNN section [47].

2.3.4 Long short-term memory (LSTM):

RNN (Recurrent Neural Network) is a class of artificial neural networks which is used to identify patterns in sequential data. Therefore, RNN can take time and sequence into account, because the RNN possesses two forms of input, the present input and the input from the recent past. The key difference between the RNN to the feed-forward network is that they have a feedback loop connected to their past decisions.

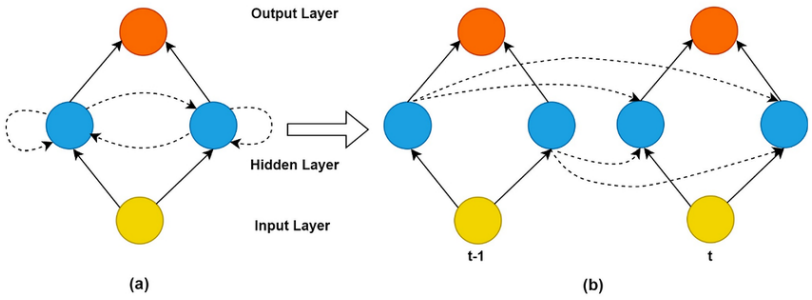

Figure 2.5: Architecture of (a) RNN, (b) RNN over a time step [50]

From Fig. 2.6, it can be seen that at a certain time t, the recurrent hidden layer neurons have input not only from the input layer x_t but also from their own previous instance h_{t-1}, i.e., from h_{t-1}. So, the output is the combination of the present and the past. The process can be represented as described by Equations (2.26) and (2.27).

$$h_t = f\left(W_{hx}x_t + W_{hh}h_{t-1} + b_h\right) \tag{2.26}$$

$$y_t = g\left(W_{yh} h_t + b_y\right) \tag{2.27}$$

Where:

- x_t is the input to the RNN at time t,
- h_t is the state of the hidden layer at time t,
- h_{t-1} is the state of the neural network at time $t-1$,
- b_h is the bias of the hidden layer,
- b_y is the bias of the output,
- W_{hx} are the weights between the hidden and the input layer,
- W_{hh} are the weights of the hidden layer at time $t-1$ and the hidden layer at time t.

RNN is trained across the time steps using backpropagation through time (BPTT) . However, because of the multiplication of gradients at time steps the gradient value becomes smaller and smaller or it gets larger and larger and as a result the RNN learning process encounters the issue of gradient vanishing or gradient exploding. Due to the issue of vanishing and exploding gradients, RNNs are used in limited applications. This issue is solved by using the LSTM (Long Short-Term Memory) which includes a memory cell that replaces the hidden RNN units [50].

Long short-term memory (LSTM) networks are a type of recurrent neural network (RNN) designed to overcome the vanishing gradient problem and capture long-range dependencies in sequential data. LSTMs contain memory cells that can maintain information over time, making them well-suited for tasks involving sequential data such as time series forecasting, natural language processing, and speech recognition.

1. **LSTM cell**:
    - The LSTM cell consists of several gates, including input gate (i), forget gate (f), output gate (o), and cell state (c). These gates regulate the flow of information through the cell.

- The computation within an LSTM cell is governed by the following equations [51]:
- **Forget Gate**:

$$f_t = \phi(W_f \cdot [h_{t-1}, x_t] + b_f) \tag{2.28}$$

- **Input Gate**:

$$i_t = \phi(W_i \cdot [h_{t-1}, x_t] + b_i) \tag{2.29}$$

- **Candidate Cell State**:

$$\tilde{c}_t = \tanh(W_c \cdot [h_{t-1}, x_t] + b_c) \tag{2.30}$$

- **Update Cell State**:

$$c_t = f_t \cdot c_{t-1} + i_t \cdot \tilde{c}_t \tag{2.31}$$

- **Output Gate**:

$$o_t = \phi(W_o \cdot [h_{t-1}, x_t] + b_o) \tag{2.32}$$

- **Hidden State**:

$$h_t = o_t \cdot \tanh(c_t) \tag{2.33}$$

Where h_t is the hidden state at time t, x_t is the input at time t, W and b are the weight matrices and bias vectors respectively, and ϕ denotes the sigmoid activation function.

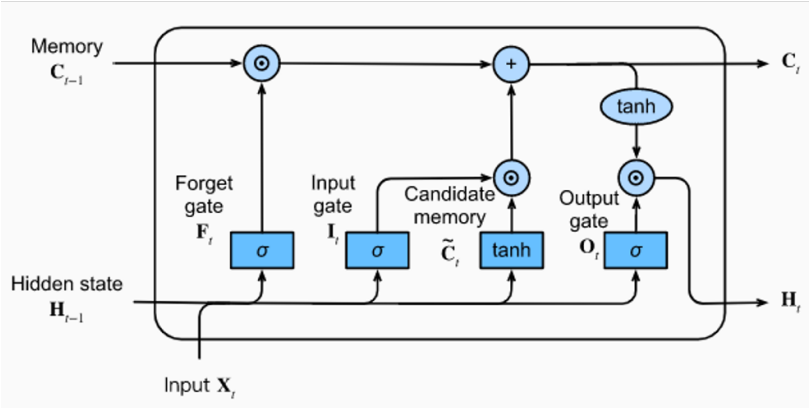

Figure 2.6: LSTM Cell Architecture [51]

2. **Learning Process**:

    - LSTMs are trained using backpropagation through time (BPTT), where the error is propagated backward through time to update the network parameters. Gradient clipping is often applied to mitigate exploding gradients.

3. **Error Function**:

    - The error function, typically mean squared error (MSE) or cross-entropy loss, quantifies the discrepancy between the predicted output and the actual target values.

4. **Optimizer**:

    - Common optimizers such as stochastic gradient descent (SGD), Adam, or RMSprop are used to update the network parameters based on the computed gradients during backpropagation.

LSTMs have demonstrated superior performance in various sequence modeling tasks compared to traditional RNNs, particularly in capturing long-term dependencies and handling vanishing gradients.

2.4 Conclusion

By integrating signal-based and AI-based approaches, a robust diagnostic framework can be established for bearing fault detection in induction motors. Signal-based methods provide a foundational understanding of the motor's physical condition, while AI-based approaches leverage this information to achieve high-precision fault detection and classification. This integrated approach facilitates early detection of anomalies, accurate fault diagnosis, and proactive maintenance, ultimately enhancing the reliability and efficiency of industrial machinery. Analysis of the previous work has allowed us to identify the following research gap:

- Very few research work have focused on the fault detection of the bearings on the fixed speed using only current signal in induction motors .

- Second to our best knowledge this is the first attempt to diagnose the bearing faults of the induction motor in variable speed operation

In the following chapters, the dataset and the methodology employed for bearing fault diagnosis will be discussed in detail.

Chapter 3

Datasets description

3.1 Introduction

In this chapter, we delve into the datasets utilized in our research, providing a comprehensive overview of their characteristics, the methods employed for their collection, and the insights gleaned from exploratory data analysis. The two primary datasets utilized in this study are the vibration datasets and the current dataset. Understanding the intricacies of these datasets is crucial for interpreting our findings.

3.2 Vibration dataset

3.2.1 Overview

Over the last decade, data from the case western reserve university (CWRU) bearing data center has become a standard reference used to test these algorithms. The data set provided by the case western reserve university (CWRU) bearing data center [52] has become such a standard reference in the bearing diagnostics field, with the authors counting 41 papers using the CWRU data published in mechanical systems and signal processing between 2004 and early 2015 .

3.2.2 Data collection process

The test rig described consists of a 2 hp reliance electric motor connected to a shaft, which is equipped with a torque transducer and an encoder. Torque is applied to the shaft using a dynamometer and electronic control system. The motor drives the shaft, and faults of varying diameters (ranging from 0.007 to 0.021 inches or 0.18 to 0.71 mm) are seeded on the drive-end and fan-end bearings.

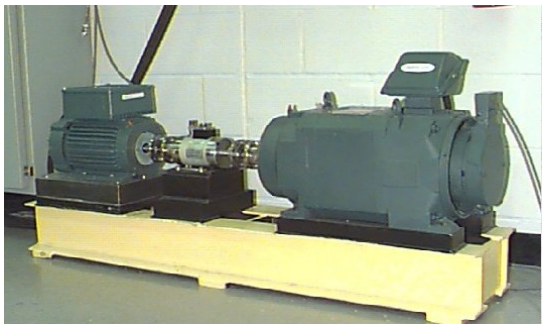

Figure 3.1: CWRU bearing test rig [52]

These faults are created using electro-discharge machining (EDM) and are seeded on the rolling elements as well as on the inner and outer races of the bearings. Each faulty bearing is then separately reinstalled on the test rig. The rig is operated at a constant speed with motor loads ranging from 0 to 3 horsepower, corresponding to approximate motor speeds of 1797 to 1720 rpm.

During the tests, acceleration is measured in the vertical direction on the housing of the drive-end bearing (DE). In some cases, acceleration is also measured vertically on the fan-end bearing housing (FE) and on the motor supporting base plate (BA). The sample rates used for measurement at 48 kHz.

3.2.3 Dataset description

The data set is grouped into four groups, within each group there are data sets for rolling element faults and inner and outer race faults, with the outer race faults themselves grouped into three categories according to the fault position relative to the load zone: 'centred' (fault in the 6.00 o'clock position), 'orthogonal' (3.00 o'clock) and 'opposite' (12.00 o'clock). It should be noted here that the only load borne by the bearings (in theory) is the static gravitational load from the weight of the shaft and any attached components, there is evidence that there could be a dynamic load superimposed on this static load. The data sets are further categorised by fault size (0.007 to 0.021") and motor load (0 to 3 hp) ,as illustrated in the table 3.1[52]

Table 3.1: 48k drive end bearing fault data

Fault Diameter	**Motor Load (HP)**	**Approx. Motor Speed (rpm)**	**Inner Race**	**Ball**	**Outer Race Centered @6:00**	**Outer Race Orthogonal @3:00**	**Outer Race Opposite @12:00**
0.007”	0	1797	IR007_0	B007_0	OR007@6_0	OR007@3_0	OR007@12_0
	1	1772	IR007_1	B007_1	OR007@6_1	OR007@3_1	OR007@12_1
	2	1750	IR007_2	B007_2	OR007@6_2	OR007@3_2	OR007@12_2
	3	1730	IR007_3	B007_3	OR007@6_3	OR007@3_3	OR007@12_3
0.014”	0	1797	IR014_0	B014_0	OR014@6_0	*	*
	1	1772	IR014_1	B014_1	OR014@6_1	*	*
	2	1750	IR014_2	B014_2	OR014@6_2	*	*
	3	1730	IR014_3	B014_3	OR014@6_3	*	*
0.021”	0	1797	IR021_0	B021_0	OR021@6_0	OR021@3_0	OR021@12_0
	1	1772	IR021_1	B021_1	OR021@6_1	OR021@3_1	OR021@12_1
	2	1750	IR021_2	B021_2	OR021@6_2	OR021@3_2	OR021@12_2
	3	1730	IR021_3	B021_3	OR021@6_3	OR021@3_3	OR021@12_3

3.2.3.1 Bearing information

The following table presents defect frequencies associated with the drive end bearing. These frequencies are expressed as multiples of the running speed in Hertz and are crucial for identifying and analyzing potential defects within the bearing components.

Table 3.2: Defect frequencies (multiples of running speed)in Hz

Faults	**Inner Ring**	**Outer Ring**	**Cage Train**	**Rolling Element**
Defect Frequencies	5.4152	3.5848	0.39828	4.7135

The defect frequencies include those related to the inner ring, outer ring, cage train, and rolling elements, providing insights into the condition and performance of the bearing.Table 3.3 delineates the dimensions of the drive end bearing, denoting its physical size in inches. These measurements encompass the inside diameter, outside diameter, thickness, ball diameter, and pitch diameter, essential for gauging the structural characteristics and fitting requirements of the bearing.

3.2.4 Exploratory data analysis

In this section, we will conduct an exploratory data analysis of the bearing data, showing statistics for the vibration datasets loads 0,1,2,3 Hp and employing Raw Data Exploration presenting the dataset in an intuitive and insightful manner.

Table 3.3: Statistics for the vibration datasets loads 0,1,2,3 Hp

Statistic	**Load 0 Hp**	**Load 1 Hp**	**Load 2 Hp**	**Load 3 Hp**
Count	2,782,629	5,258,548	6,813,513	6,814,675
Mean	0.08997707	0.02758404	0.01376063	0.01280094
Standard Deviation	0.5496821	0.4540467	0.4900714	0.4427520
Minimum	-7.250749	-7.250749	-6.926899	-7.019547
25th Percentile	-0.07178133	-0.09682133	-0.1207883	-0.1189108
50th Percentile (Median)	0.07092923	0.02170133	0.01439446	0.01356000
75th Percentile	0.2814222	0.1469013	0.1474911	0.1441532
Maximum	7.702304	7.702304	7.323365	7.559576

Table 3.5 shows that as the load increases from 0 Hp to 3 Hp, the mean and median vibration levels decrease, indicating lower average vibrations at higher loads. The variability, indicated by the standard deviation, is slightly higher at lower loads. The minimum and maximum values show the extent of the vibration range, which remains relatively constant across different loads. The quartiles (25th, 50th, and 75th percentiles) also reflect this trend of decreasing central values with increasing load.

3.2.4.1 Raw data exploration

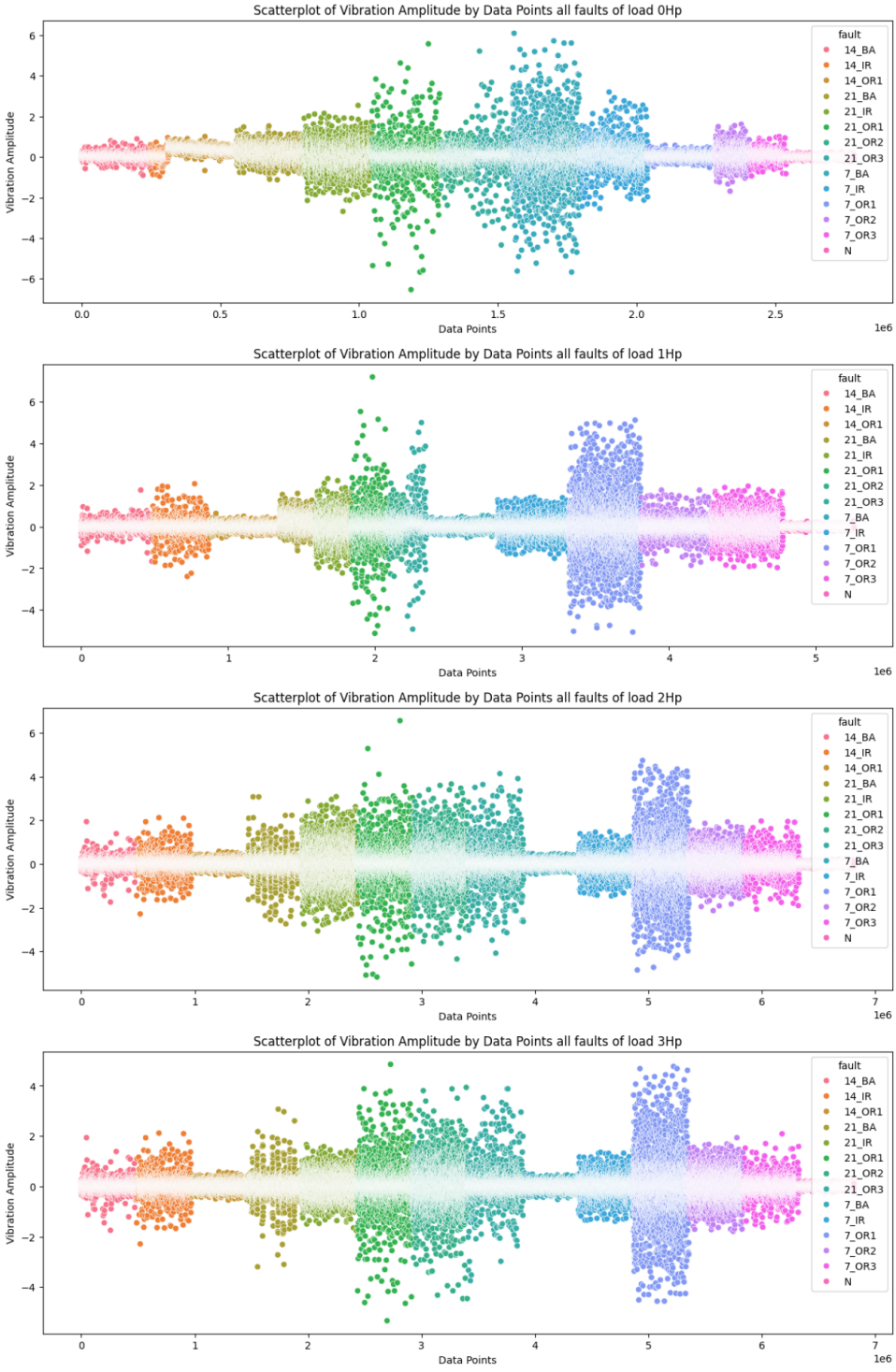

Figure 3.2: Scatterplot of vibration amplitude by data points 0hp,1hp,2hp,3hp loads

The scatter representation of raw accelerometer data provides an illuminating glimpse into the intricate behavior of 14 fault class severities within bearing components across Four distinct loading scenarios: Load 0hp, Load 1hp, Load 2 hp, and Load 3hp.

Observations gleaned from the raw data scatter plots reveal intriguing patterns. For instance, the "N" (normal) bearing consistently exhibits minimal vibration levels across all loading conditions. Conversely, the "7_BA" bearing, featuring a 0.007-inch roller-element fault, showcases pronounced vibration spikes particularly evident during the no-load scenario. Notably, these spikes diminish under load, suggestive of a nuanced interplay between operating conditions and vibration characteristics. This phenomenon may be attributed to the alteration in motor operational dynamics, where the absence of external loads during no-load conditions permits heightened vibration levels due to reduced damping forces, potentially accentuating fault manifestation.

Of paramount significance are fault labels marked by the largest depth damage, notably 0.021 inches (21_BA, 21_IR, 21_OR1, 21_OR2, 21_OR3), characterized by conspicuous vibration spikes regardless of loading scenarios. Conversely, fault labels with depths of 0.014 and 0.007 inches prove less discernible based solely on vibration signatures. This disparity could stem from the critical positioning of faults within the bearing or motor system, with certain locales predisposed to heightened vibration generation owing to proximity to other components or unique force distribution dynamics. Moreover, faults with larger depth damage potentially exert a more pronounced influence on the system's natural frequencies, altering stiffness and mass properties to a greater extent, consequently yielding larger vibration shifts.

Further in-depth analysis is warranted to unravel the underlying intricacies governing these vibration patterns and to elucidate potential fault origins within the roller elements.

3.3 Current Dataset

3.3.1 Overview

The current dataset focused on the dynamics of rotating machines under various operating conditions. This dataset includes time-series data of the driving currents of rotating machinery across different environments. Data was collected using instrumentation with three current transformers (CTs), following the standards of the International Organization for Standardization (ISO). This dataset is a valuable resource for validating and benchmarking methods in fault diagnosis for rotating machinery. Available on Mendeley Data, it supports progress in machine health monitoring and predictive maintenance [53].

3.3.2 Data collection process

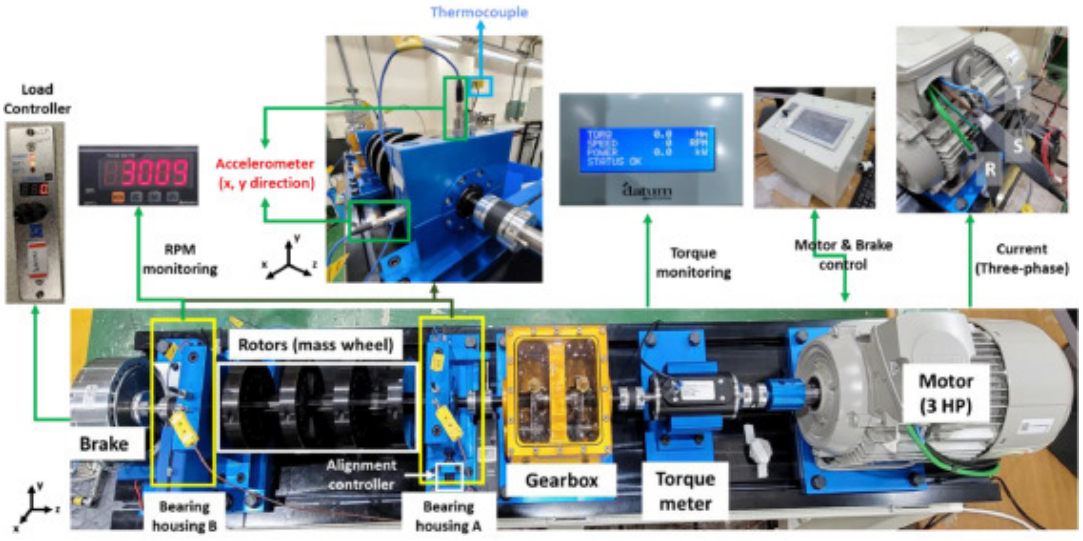

Figure 3.3: Layout of the rotating machine testbed and its components [53].

The rotating machine testbed includes a three-phase induction motor, torque meter, gearbox, bearing housings A and B, rotors, and a hysteresis brake, as depicted in Fig. 3.3. The induction motor, produced by SIEMENS, is a four-pole AC motor with a power rating of 3 horsepower (HP). It operates at 380 V, 60 Hz, with a rated speed of 1770 rpm. The gearbox amplifies the rotational

speed by a factor of 2.07, reaching up to 3663 rpm. To prevent signal overlap with the 60 Hz driving frequency, the system was run at 3010 rpm.

A hysteresis brake (AHB-3A) from Valid Magnetic Ltd. was used to apply load to the machine, and a torque meter (M425) from Datum Electronics measured the load. The simulated loads in the dataset are 0 Nm, 2 Nm, and 4 Nm.

To measure the current in the three-phase motor, three Hioki CT6700 current transformers (CTs) were utilized, installed on the U-phase, V-phase, and W-phase of the motor. Current data was collected using an NI9775 C Series Digitizer Module, with a sampling frequency of 100 kHz for variable speed operation and 25.6 kHz for fixed speed operation.

3.3.3 Dataset description

This dataset consists of two parts: varying load conditions, and varying speed conditions.
In part 1, this dataset contains data related to most of the major faults (bearing, shaft, and rotor faults) that can occur in rotating machines. Therefore, this dataset can be used to verify the performance of the newly developed rotating machine fault diagnosis methods based on rotor dynamics theories.

In part 2, this dataset was acquired from rolling element bearing under varying speed conditions (680 RPM to 2460 RPM). Three different types of faults, including inner race fault, outer race fault, and ball fault, were seeded. This data consists current data.

·Most of the fault diagnosis methods are proposed for extracting fault features with steady speed and cannot be directly used with varying speed conditions . Practically, in wind turbines, bearing does not operate at a steady speed due to load fluctuations . To solve these problems, eliminating the effect of varying speed condition such as order tracking are conducted, however, it needs to collect synchronized speed data with vibration.

Tables 1 and 2 provide descriptions of the motor current data according to the operating and health conditions of the rotating machine.

Table 3.4: Description of fault data [53]

Fault location	**Fault types**	**Fault severity**	**Length (second)**	**Load (Nm)**	**Rotating speed (RPM)**	**Sampling rate (kHz)**
-	Normal	-	120	0, 2, 4	3010	25.6
Bearing housing A	Inner	0.3 mm	60	0, 2, 4	3010	25.6
Bearing housing A	Inner	1.0 mm	60	0, 2, 4	3010	25.6
Bearing housing A	Inner	3.0 mm	60	0, 2, 4	3010	25.6
Bearing housing A	Outer	0.3 mm	60	0, 2, 4	3010	25.6
Bearing housing A	Outer	1.0 mm	60	0, 2, 4	3010	25.6
Bearing housing A	Outer	3.0 mm	60	0, 2, 4	3010	25.6

Table 3.5: Motor current from bearing under varying speed conditions [53]

Fault location	**Fault types**	**Length (second)**	**Load (Nm)**	**Rotating speed (RPM)**	**Sampling rate (kHz)**
	Normal	2,100 (300 per file)	0	680 $\sim$ 2460	100
Bearing housing B	Inner	2,100 (300 per file)	0	680 $\sim$ 2460	100
	ball	2,100 (300 per file)	0	680 $\sim$ 2460	100
	Outer	2,100 (300 per file)	0	680 $\sim$ 2460	100

3.3.4 Exploratory data analysis

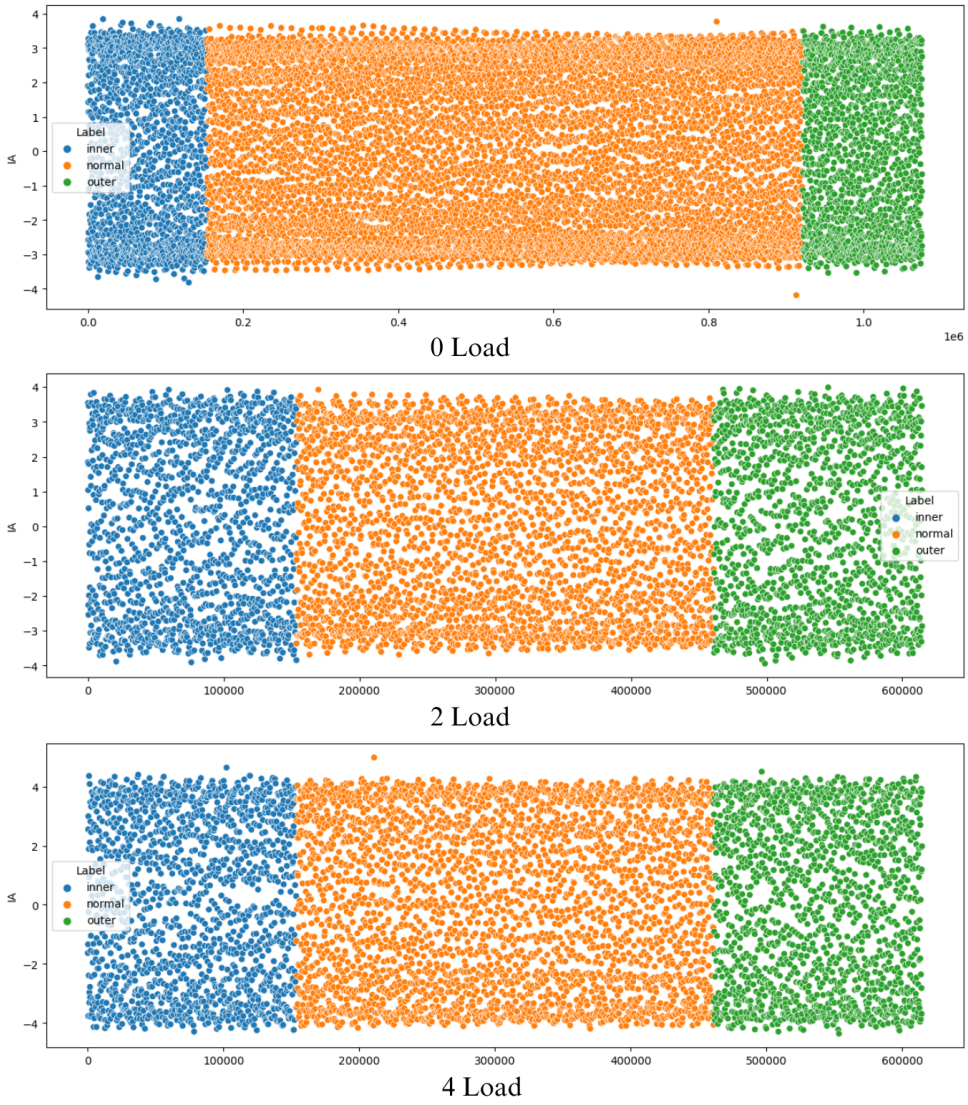

Figure 3.4: Scatterplot of current Amplitude by Data Points 0m, 2m, 4Nm loads

The first impression form the scatter plot are that the data is not balanced in all loads cases, so that it appears that the no anomaly case has more data set and it is more noticeable in the load case of 0 load. Addtiional to that the datasets are not same size the load 0 data set is huge compared to the others. The diffrence betwen the features it is clar that it is diffuclt to diffrentiate between them.

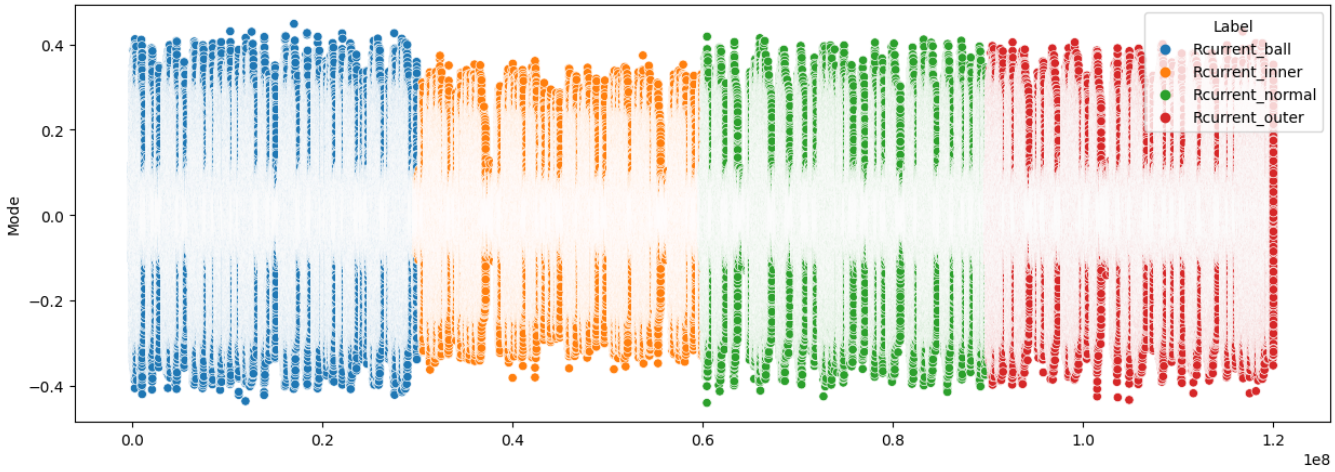

Figure 3.5: Scatterplot of current Amplitude by Data Points variable speed operation

The variable speed operation current dataset in the inner race faults case where it is noticeable that the lowest current amplitudes. the ball faults are also having the highest amplitude picks and spikes.

3.4 Conclusion

This chapter discussed the essential points about the used dataset within this work.In fact two datasets has been discussed within this chapter,in order to use them for the bearing faults diagnosis further signal processing and data processing is needed,and that is discussed in the following chapter where their will be also the implementation of the model and the results.

Chapter 4

Bearing faults classification

4.1 Introduction

This chapter presents the methodology employed to detect and classify bearing faults in induction motors. The study utilizes three distinct datasets, as described in Chapter 03: the vibration dataset and the current datasets in both operation modes fixed speed variable load and variable speed fixed load.The processing steps for each dataset are detailed, preparing them for analysis by signal processing algorithms and artificial intelligence models to extract the necessary features for fault detection and classification. Subsequently, the results are presented and analyzed, concluding with a comparative study between the vibration-based approach and the current-based approach.

4.2 Vibration signal dataset

4.2.1 Principle of detection

The vibration signal is the most commonly used signal for detecting bearing faults because the fault signatures appear clearly, resulting in minimal preprocessing. Initially, The presence of fault frequencies within the signal is checked using the Fast Fourier Transform (FFT). This step helps determine the appropriate preprocessing required, such as filtering or transformation. Following this, the classifier is built using time series data. The data is segmented into chunks using an appropriate window and stride length, which are selected based on T-distributed Stochastic Neighbor Embedding (T-SNE) intensive observation and the resultant accuracy of the model. Each model's performance is evaluated and tuned to ensure optimal results. The Fig 4.1 illustrates the method used:

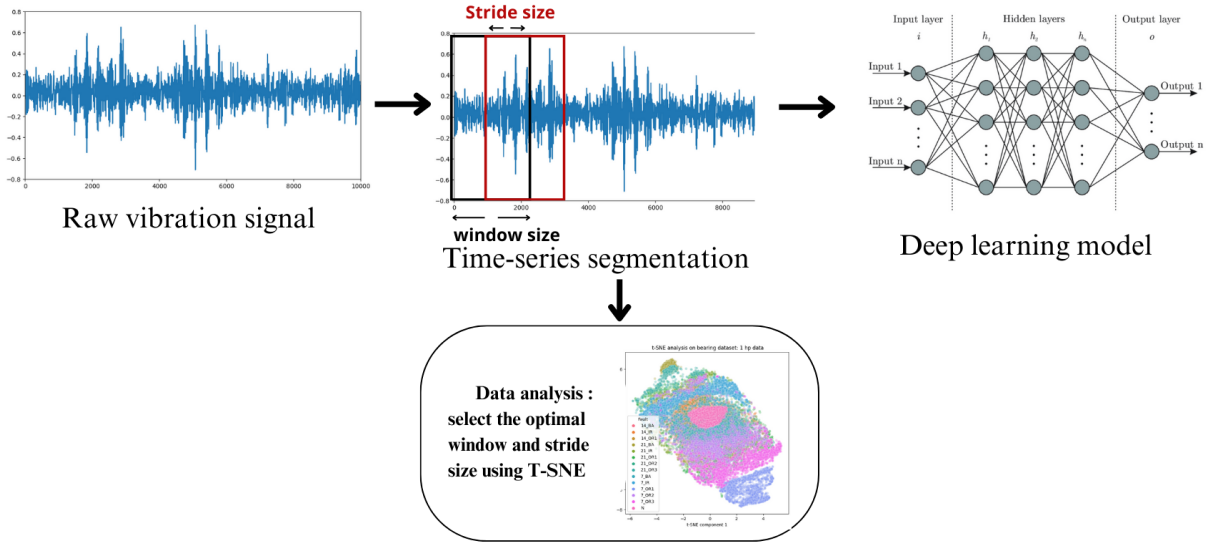

Figure 4.1: Bearing-fault diagnosis using vibration signal methodology.

4.2.2 Data preprocessing

In this section, the data preprocessing techniques employed to ensure the optimal performance of our artificial intelligence model in detecting and classifying bearing faults will be elucidated. Achieving accurate predictions and effective feature extraction hinges on the quality of our data and the selection of appropriate data chunks or segments for model training.

First, Fast Fourier Transform (FFT) was applied to the vibration data to confirm the presence of bearing faults. The FFT helps in transforming the time-domain signals into the frequency domain, making it easier to identify characteristic fault frequencies.

To further enhance our data preprocessing pipeline and address the challenge of selecting the appropriate data chunks for model training.

T-SNE (T-distributed stochastic neighbor embedding): a powerful dimensionality reduction technique, was leveraged. T-SNE facilitates the visualization of high-dimensional data in lower-dimensional space, thereby enhancing our understanding of the underlying patterns and relationships within the dataset.

4.2.3.1 Fast fourier transform (FFT)

Employing FFT (Fast Fourier Transform) to extract frequency information and identify potential faults.Our objective is to uncover hidden insights and patterns embedded within the data we utilized the Defect Frequencies, multiples of the running speed in Hertz, associated with each fault to detect and verify the presence of faults within the bearing. By focusing on these specific frequencies, we aimed to discern the distinct signatures indicative of various fault types.

The results of our analysis are as follows:

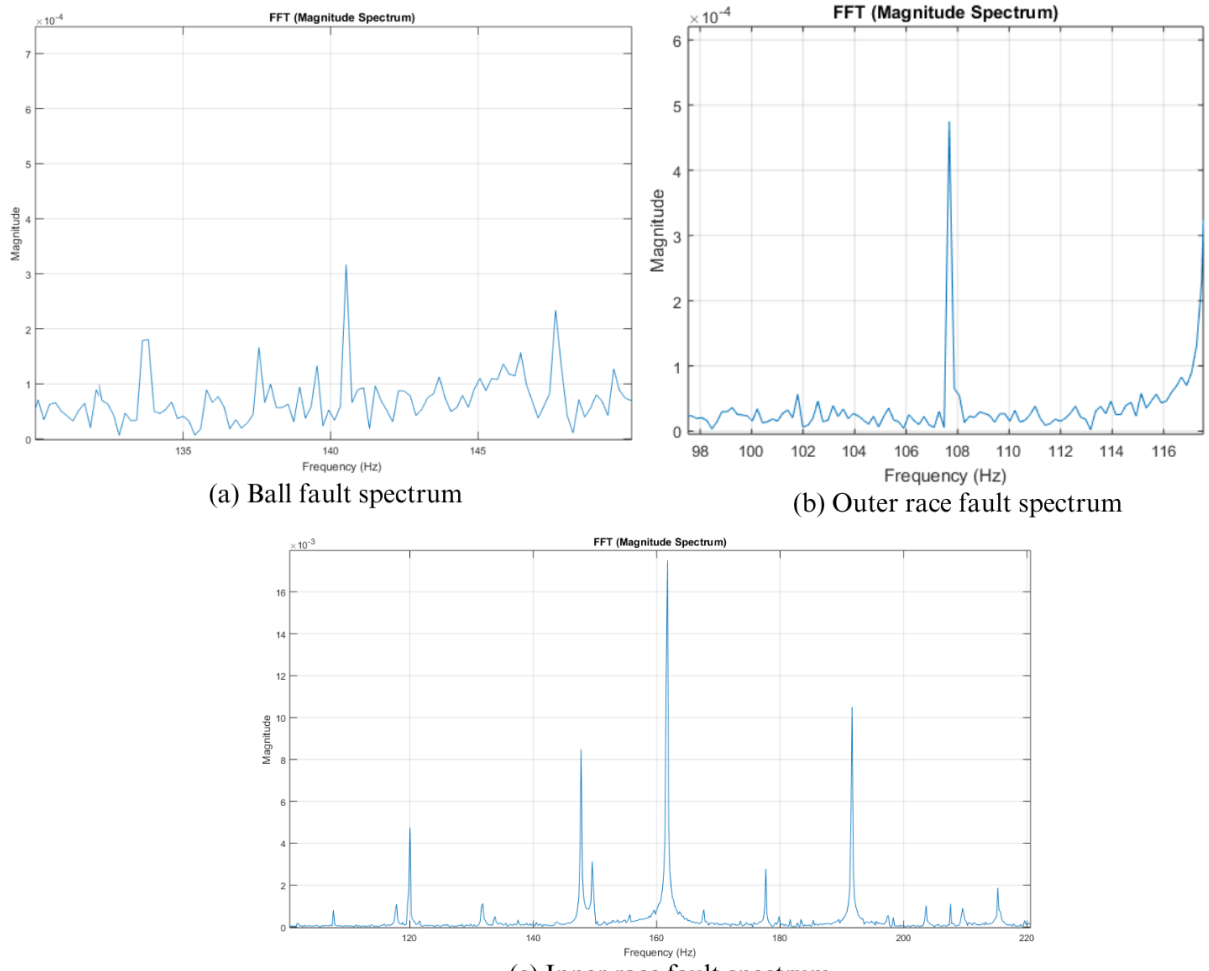

(a) Ball fault spectrum

(b) Outer race fault spectrum

(c) Inner race fault spectrum

Figure 4.2: FFT magnitude sepctrum of 0hp ball fault data.

- Ball fault frequency: 141 Hz.

- Inner fault frequency: 163 Hz.
- Outer fault frequency: 108 Hz.

Using Fast fourier transform to analyse the different bearing faults (ball, inner race and outer race faults) frequencies and check its existence.We have identified distinct frequency peaks associated with different types of bearing faults described in Table 3.2 .These fault-specific FFT fig 4.2, coupled with their corresponding special fault frequencies, confirm the presence of the bearing faults signature within the vibration signal. By detecting deviations from normal operating frequencies, we can start building our model to accurately identify and classify the bearing faults.

4.2.3.2 Time-series segmentation:

Time-series segmentation is a method of time-series analysis in which an input time-series is divided into a sequence of discrete segments in order to reveal the underlying properties of its source,as illustrated in figure 4.3.

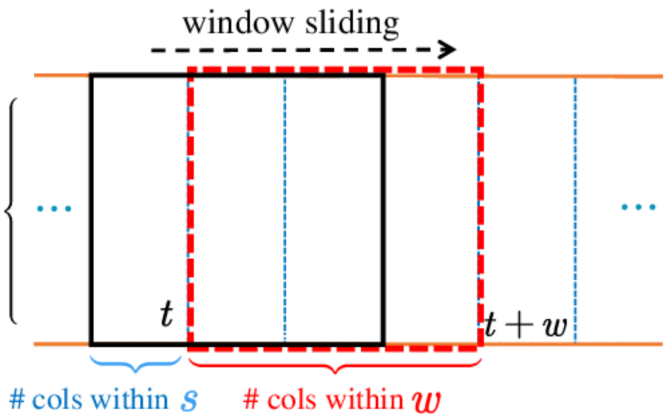

Figure 4.3: The sliding window for the row-signal.

W is the window size , **S** is the stride size .

To choose the optimal window size for capturing the features within the signal, we use t-SNE (t-Distributed Stochastic Neighbor Embedding) to visualize the obtained segments. This visualization helps us identify distinct clusters and patterns within the signal.

Based on the t-SNE visualization, we then select three major window sizes: the maximum, minimum, and average values. The process is detailed in the following section.

4.2.3.3 T-SNE (T-distributed stochastic neighbor embedding):

T-SNE, short for T-distributed stochastic neighbor embedding, is a nonlinear dimensionality reduction technique widely used for visualizing high-dimensional data in lower-dimensional space. Unlike traditional methods such as PCA (Principal Component Analysis), T-SNE preserves local structures and captures complex relationships between data points [54]. By transforming the original feature space into a two- or three-dimensional representation, T-SNE enables us to gain insights into the inherent structures and clusters within the data, facilitating more informed decision-making and model development.The results obtained using T-SNE will help to detect the best parameters for Time-series segmentation (window size and stride size).However the optimal size of the T-SNE differs from algorithm to algorithm so we select three major window sizes: the maximum, minimum, and average values.

the optimal parameters obtained from tnse are shown in the fig 4.4 :

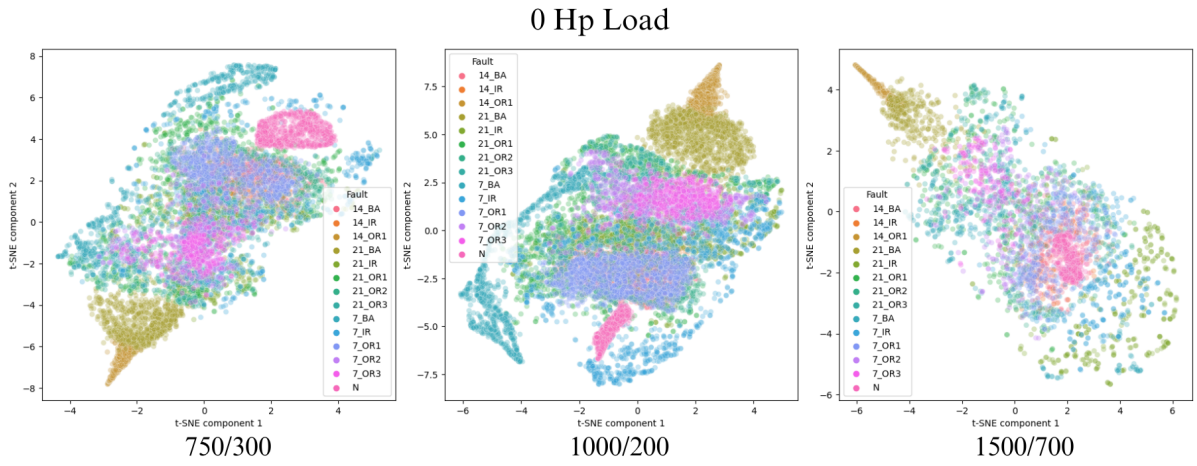

Figure 4.4: 0 Hp Load data visualization using T-SNE algorithm

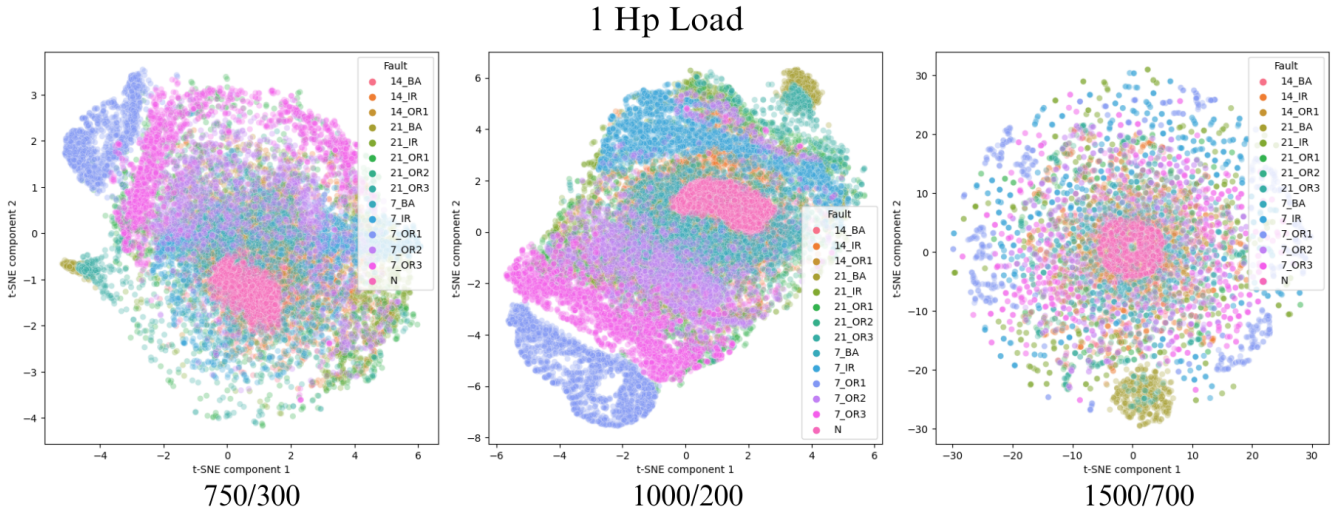

Figure 4.5: 1 Hp Load data visualization using T-SNE algorithm.

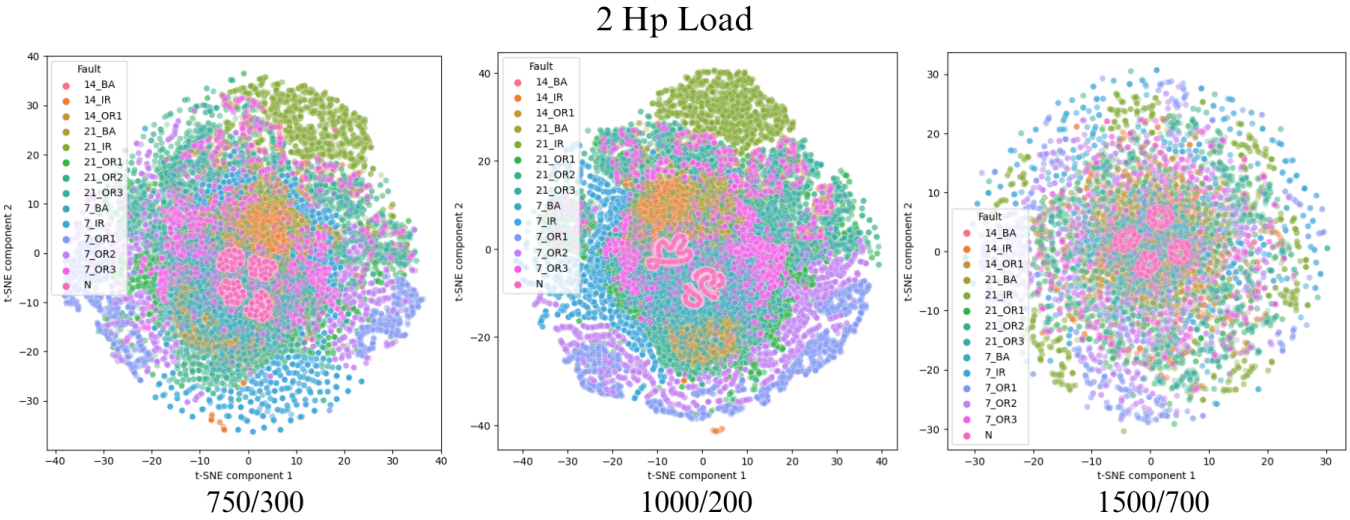

Figure 4.6: 2 Hp Load data visualization using T-SNE algorithm.

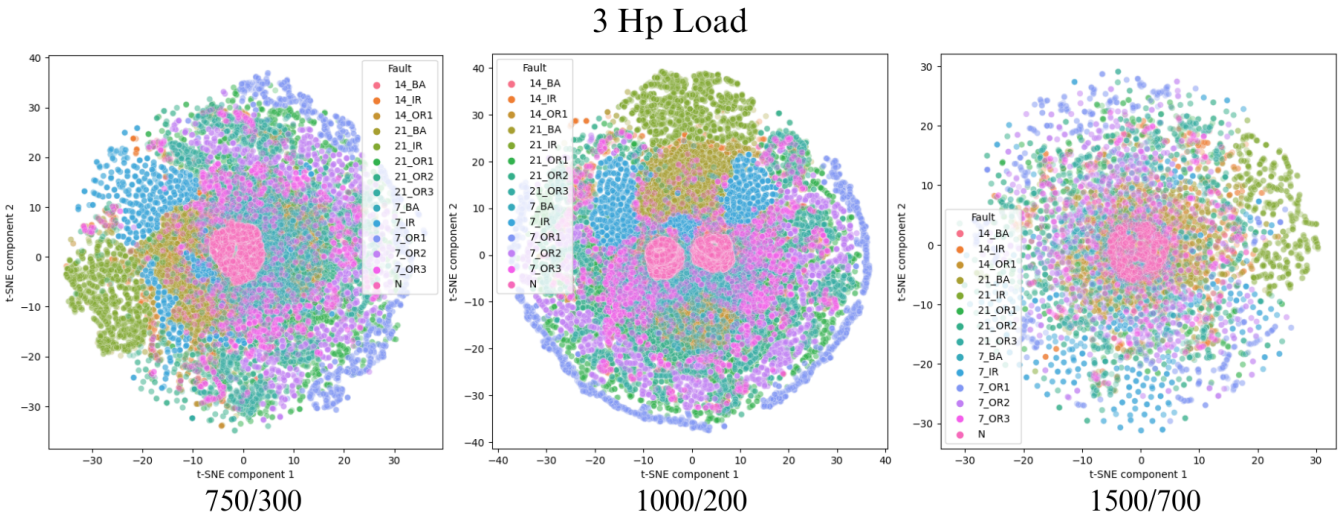

Figure 4.7: 3 Hp Load data visualization using T-SNE algorithm.

The exploration in Figures (4.5-4.7) suggests that the underlying structure of the data is complex, with multiple overlapping patterns of variation that are difficult to distinguish using T-SNE. In all load conditions, the data classes with a window size of 750 start to overlap significantly and cluster together. With a window size of 1500, the overlap increases, but the data becomes more spread out and mixed. A window size of 1000 appears to be optimal, where the data classes are well arranged and separated, though there is still some overlap between two or three classes, which remains distinguishable. After numerous experiments, we determined the best stride sizes and decided to keep the three major window sizes without committing to just one. This approach allows us to make the final decision within the model experiments, as each algorithm has its own input specifications.

These factors may be difficult to fully capture using T-SNE, which relies on the assumption of a low-dimensional structure within the data. Furthermore, T-SNE is known to be relatively weak for distinguishing between classes within a dataset. This is because T-SNE is primarily designed to preserve the local relationships between data points rather than the global relationships between classes.

4.2.3 Results and discussion

In this subsection, the deep learning models employed for classifying bearing faults are described. Four algorithms were utilized for training: Artificial Neural Network (ANN), one-dimensional Convolutional Neural Network (1D-CNN), 1D-CNN with multiple kernel sizes, and Long Short-Term Memory (LSTM). Their respective results are showcased and performances evaluated to determine optimal parameters and the most effective model for classification.In evaluating model performance, performance metrics and the classification report were employed , focusing on weighted precision, weighted recall, and weighted F1-score. The definitions and equations for these metrics[55] are as follows:

a) Weighted precision

Weighted precision is the precision of the classifier taking into account the number of samples in each class. The precision for class i is given by:

$$P_i = \frac{TP_i}{TP_i + FP_i} \tag{4.1}$$

where TP_i is the number of true positives for class i,FP_i is the number of false positives for class i. The weighted precision is given by:

$$\text{Weighted Precision} = \frac{\sum_{i=1}^{n}(P_i \cdot N_i)}{\sum_{i=1}^{n} N_i} \tag{4.2}$$

where P_i is the precision for class i and N_i is the number of true instances for class i.

ts of the Variational Mode Decomposition (VMD).Following this, the classifier is built using time series data. The data is segmented into chunks using an appropriate window and stride length, the resultant accuracy of the model. Each model's performance are evaluated and tuned to ensure optimal results,figure 4.12 illustrate the method used :

4.3 Conclusion

The analysis of bearing fault detection using vibration and current signals demonstrates the effectiveness of advanced neural network models, particularly 1D-CNN and its multi-kernel size variant, in achieving high accuracy across different operational conditions. The 1D-CNN multi-kernel size model consistently outperformed other models such as ANN and LSTM in the vibration dataset, with accuracies reaching up to 99.95% under various load conditions. This superior performance is attributed to the model's ability to extract diverse features through different kernel sizes, which enhances its capability to capture intricate patterns in the data.

Comparative analysis with previous works highlights the advancements made in this study. Unlike earlier methodologies that relied on extensive preprocessing techniques, and signal decomposition, our approach minimized preprocessing, thereby preserving more of the original data's features. This methodological shift not only improved the accuracy but also simplified the data processing pipeline.

For the current signal dataset, the fixed speed operation results indicated that the 1D-CNN models maintained high accuracy, with the highest being 99.88% at 0 Nm load. This success underscores the efficacy of combining 1D-CNN with Variational Mode Decomposition (VMD) to handle complex fault patterns by effectively decomposing the signal and addressing boundary effects. However, the variable speed operation presented more challenges, yet the models still achieved commendable accuracies, with the 1D-CNN model reaching up to 99.36%.

The methodologies employed for both vibration and current signals involved initial fault frequency analysis using Fast Fourier Transform (FFT), followed by segmentation and classification using time series data. For the vibration signals, preprocessing techniques like FFT and t-SNE were crucial in enhancing feature extraction and visualization, leading to improved model performance.

Overall, this study's methodology and results contribute significantly to the field of bearing fault detection, demonstrating that advanced neural network models, particularly 1D-CNN with multi-kernel sizes, can achieve high accuracy with minimal preprocessing. These findings suggest that further exploration of neural network architectures and preprocessing techniques can continue to improve fault detection capabilities in industrial applications.

Bibliography

[1] P. Krause, *Analysis of Electric Machinery*. Electrical Engineering Series, McGraw-Hill, 1986.

[2] S. Karmakar, S. Chattopadhyay, M. Mitra, and S. Sengupta, *Induction Motor and Faults*, pp. 7–28. Singapore: Springer Singapore, 2016.

[3] P. K. Chandra, "Identification of different parts for a three phase induction motor.." `https://electricalnotebook.com/parts-of-3ph-induction-motor/`, 2024. Accessed: 2024-06-12.

[4] P. Sen, *Principles of Electric Machines and Power Electronics*. Wiley, 1989.

[5] D. Molnár, M. Blatnický, and J. Dižo, "Design of the power of an electric lifting motor for a single girder bridge crane with a 500 kg load capacity," *Transport technic and technology*, vol. 17, no. 2, pp. 23–29, 2021.

[6] M. Say, *The Performance and Design of Alternating Current Machines: Transformers, Three-phase Induction Motors and Synchronous Machines*. Pitman's engineering degree series, Pitman, 1948.

[7] J. S. David Greenfield, "Motors: The core of automation," Sept 2023.

[8] D. Kothari and I. Nagrath, *Electric Machines*. Electric power systems, Tata McGraw-Hill, 2004.

[9] "Ieee recommended practice for the design of reliable industrial and commercial power systems (gold book)," *IEEE Std 493-1997 [IEEE Gold Book]*, pp. 1–464, 1998.

[10] "Report of large motor reliability survey of industrial and commercial installations, part i," *IEEE Transactions on Industry Applications*, vol. IA-21, no. 4, pp. 853–864, 1985.

[11] O. Thorsen and M. Dalva, "A survey of faults on induction motors in offshore oil industry, petrochemical industry, gas terminals, and oil refineries," *IEEE Transactions on Industry Applications*, vol. 31, no. 5, pp. 1186–1196, 1995.

[12] G. Singh and S. Ahmed Saleh Al Kazzaz, "Induction machine drive condition monitoring and diagnostic research—a survey," *Electric Power Systems Research*, vol. 64, no. 2, pp. 145–158, 2003.

[13] P. Albrecht, J. Appiarius, R. McCoy, E. Owen, and D. Sharma, "Assessment of the reliability of motors in utility applications - updated," *IEEE Transactions on Energy Conversion*, vol. EC-1, no. 1, pp. 39–46, 1986.

[14] A. Bonnett and G. Soukup, "Analysis of rotor failures in squirrel-cage induction motors," *IEEE Transactions on Industry Applications*, vol. 24, no. 6, pp. 1124–1130, 1988.

[15] N. Sarma, P. Tuohy, and S. Djurovic, *Condition monitoring of rotating electrical machines*. 09 2022.

[16] P. Tavner, L. Ran, J. Penman, and H. Sedding, "Condition monitoring of rotating electrical machines," *Bibliovault OAI Repository, the University of Chicago Press*, 01 2008.

[17] A. H. Bonnett and G. C. Soukup, "Cause and analysis of stator and rotor failures in 3-phase squirrel cage induction motors," *Conference Record of 1991 Annual Pulp and Paper Industry Technical Conference*, pp. 22–42, 1991.

[18] M. D. H. Wahba, "Using motor current signature analysis to detect the number of broken rotor bars in induction motors." `https://masterbuh.com/storage/editor/files/10738a28cf377cc141624aafb9fb06d5`. Accessed: 2024-06-12.

[19] Y. Soufi, B. Tahar, M.-F. HARKAT, and H. Merabet, "Detection of broken bars in squirrel cage induction motor," in *2009 International Conference on Information and Communication Technologies: From Theory to Applications (ICTTA)*, Nov 2009.

[20] A. Bellini, F. Filippetti, C. Tassoni, and G.-A. Capolino, "Advances in diagnostic techniques for induction machines," *Industrial Electronics, IEEE Transactions on*, vol. 55, pp. 4109 – 4126, 01 2009.

[21] M. Sintoni, A. Bellini, D. Forlivesi, and C. Bianchini, "Rotor fault detection of induction machines with optimal wavelet transform," in *2021 IEEE Workshop on Electrical Machines Design, Control and Diagnosis (WEMDCD)*, pp. 283–288, 2021.

[22] A. Bonnett and G. Soukup, "Cause and analysis of stator and rotor failures in 3-phase squirrel cage induction motors," in *Conference Record of 1991 Annual Pulp and Paper Industry Technical Conference*, pp. 22–42, 1991.

[23] D. Dorrell, W. Thomson, and S. Roach, "Analysis of airgap flux, current and vibration signals as a function of the combination of static and dynamic airgap eccentricity in 3-phase induction motors," in *IAS '95. Conference Record of the 1995 IEEE Industry Applications Conference Thirtieth IAS Annual Meeting*, vol. 1, pp. 563–570 vol.1, 1995.

[24] M. Bradford, "Unbalanced magnetic pull in a 6-pole induction motor," *Proceedings of the IEE*, November 1968.

[25] M. Drif and A. J. M. Cardoso, "Airgap-eccentricity fault diagnosis, in three-phase induction motors, by the complex apparent power signature analysis," *IEEE Transactions on Industrial Electronics*, vol. 55, no. 3, pp. 1404–1410, 2008.

[26] D.-H. Hwang, K.-C. Lee, J.-H. Lee, D.-S. Kang, J.-H. Lee, and K.-H. Choi, "Analysis of a three phase induction motor under eccentricity condition," in *31st Annual Conference of IEEE Industrial Electronics Society, 2005. IECON 2005.*, pp. 5 pp.–, 2005.

[27] "Deep groove ball bearing animated." `https://savree.com/en/encyclopedia/deep-groove-ball-bearing-animated`. Accessed: 2024-06-12.

[28] J. Brändlein, P. Eschmann, L. Hasbargen, and U. Merkle-Eschmann, *Ball and Roller Bearings: Theory, Design, and Application*. Wiley, 1985.

[29] R. Schoen, T. Habetler, F. Kamran, and R. Bartfield, "Motor bearing damage detection using stator current monitoring," *IEEE Transactions on Industry Applications*, vol. 31, no. 6, pp. 1274–1279, 1995.

[30] A. Siddique, G. Yadava, and B. Singh, "A review of stator fault monitoring techniques of induction motors," *IEEE Transactions on Energy Conversion*, vol. 20, no. 1, pp. 106–114, 2005.

[31] S.-B. Lee, R. Tallam, and T. Habetler, "A robust, on-line turn-fault detection technique for induction machines based on monitoring the sequence component impedance matrix," in *2001 IEEE 32nd Annual Power Electronics Specialists Conference (IEEE Cat. No.01CH37230)*, vol. 4, pp. 2217–2223 vol. 4, 2001.

[32] J. Aguayo, A. Claudio, L. Vela, S. Lesecq, and A. Barraud, "Stator winding fault detection for an induction motor drive using actuator as sensor principle," in *IEEE 34th Annual Conference on Power Electronics Specialist, 2003. PESC '03.*, vol. 3, pp. 1347–1351 vol.3, 2003.

[33] T. A. Lipo. Wisconsin Power Electronics Research Center, University of Wisconsin: Madison, Wis., 2004.

[34] W. T. Thomson and R. J. Gilmore, "Motor current signature analysis to detect faults in induction motor drives - fundamentals, data interpretation, and industrial case histories," *IEEE Transactions on Industrial Electronics*, vol. 50, no. 3, pp. 634–645, 2003.

[35] T. M. Wolbank and P. E. Macheiner, "Adjustment, measurement and on-line detection of air gap asymmetry in ac machines," in *2007 European Conference on Power Electronics and Applications*, pp. 1–8, 2007.

[36] A. H. Bonnett and C. Yung, "Increased efficiency versus increased reliability," *IEEE Industry Applications Magazine*, vol. 14, no. 1, pp. 29–36, 2008.

[37] G. Wu, T. Yan, G. Yang, H. Chai, and C. Cao, "A review on rolling bearing fault signal detection methods based on different sensors," *Sensors*, vol. 22, no. 21, 2022.

[38] A. Rai and S. Upadhyay, "A review on signal processing techniques utilized in the fault diagnosis of rolling element bearings," *Tribology International*, vol. 96, pp. 289–306, 2016.

[39] R. Yan, R. X. Gao, and X. Chen, "Wavelets for fault diagnosis of rotary machines: A review with applications," *Signal Processing*, vol. 96, pp. 1–15, 2014. Time-frequency methods for condition based maintenance and modal analysis.

[40] R. Randall, "Vibration-based condition monitoring: Industrial, aerospace and automotive applications," *Vibration-based Condition Monitoring: Industrial, Aerospace and Automotive Applications*, 12 2010.

[41] P. Stoica and R. Moses, "Spectral analysis of signals," *Prentice Hall*, 01 2005.

[42] J. W. Cooley and J. W. Tukey, "An algorithm for the machine calculation of complex fourier series," *Mathematics of Computation*, vol. 19, pp. 297–301, 1965.

[43] P. Jain and S. Bhosle, "A review on vibration signal analysis techniques used for detection of rolling element bearing defects," *International Journal of Mechanical Engineering*, vol. 8, pp. 14–29, 01 2021.

[44] L. Cohen, "Time-frequency distributions-a review," *Proceedings of the IEEE*, vol. 77, no. 7, pp. 941–981, 1989.

[45] L. Ye, X. Ma, and C. Wen, "Rotating machinery fault diagnosis method by combining time-frequency domain features and cnn knowledge transfer," *Sensors*, vol. 21, p. 8168, 12 2021.

[46] Z. Xu, C. Li, and Y. Yang, "Fault diagnosis of rolling bearing of wind turbines based on the variational mode decomposition and deep convolutional neural networks," *Applied Soft Computing*, vol. 95, p. 106515, 2020.

[47] I. Goodfellow, Y. Bengio, and A. Courville, *Deep Learning*. Cambridge, Massachusetts: MIT Press, 1st ed., 2016.

[48] M. Martinez, J. Adami, R. Capelini, M. Parentoni, I. Sene, U. Brazil, U. Brazil, A. Sul, and Brazil, "The use of artificial neural networks for identification and location of defective insulators in power lines through current transformers," in *Proceedings of the IEEE International Conference on Industrial Technology*, (Lisbon, Portugal), pp. 1–6, IEEE, June 2011.

[49] S. Singh, "Convolutional neural networks." `https://medium.com/@shekhawatsamvardhan/types-of-neural-networks-convolutional-neural-networks-bd973e4fe78c`, 2024. Accessed: 2024-06-02.

[50] R. Sabir, D. Rosato, S. Hartmann, and C. Guehmann, "Lstm based bearing fault diagnosis of electrical machines using motor current signal," in *2019 18th IEEE International Conference On Machine Learning And Applications (ICMLA)*, pp. 613–618, 2019.

[51] S. Hochreiter and J. Schmidhuber, "Long Short-Term Memory," *Neural Computation*, vol. 9, pp. 1735–1780, 11 1997.

[52] Case Western Reserve University, "Bearing data center." `https://engineering.case.edu/bearingdatacenter`. Accessed: 2024-06-02.

[53] W. Jung, S.-H. Kim, S.-H. Yun, J. Bae, and Y.-H. Park, "Vibration, acoustic, temperature, and motor current dataset of rotating machine under varying operating conditions for fault diagnosis," *Data in Brief*, vol. 48, p. 109049, 2023.

[54] L. van der Maaten and G. Hinton, "Viualizing data using t-sne," *Journal of Machine Learning Research*, vol. 9, pp. 2579–2605, 11 2008.

[55] M. Sokolova and G. Lapalme, "A systematic analysis of performance measures for classification tasks," *Information Processing Management*, vol. 45, no. 4, pp. 427–437, 2009.